Wet Snow Mapping in Southern Ontario with Sentinel-1A Observations

by

Hongjing Chen

A thesis

presented to the University of Waterloo

in the fulfilment of the

thesis requirement for the degree of

Master of Science

in

Geography

Waterloo, Ontario, Canada, 2018

Author's Declaration

I hereby declare that I am the sole author of this thesis. This is a true copy of the thesis, including any required final revisions, as accepted by my examiners.

I understand that my thesis may be made electronically available to the public.

Abstract

Wet snow is defined as snow with liquid water present in an ice-water mix. It can be an indicator for the onset of the snowmelt period. Knowledge about the extent of wet snow area can be of great importance for the monitoring of seasonal snowmelt runoff with climate-induced changes in snowmelt duration. Moreover, effective monitoring wet snow cover has implications for operational hydrological and ecological applications. Spaceborne microwave remote sensing has been used to observe seasonal snow under all-weather conditions. Active microwave observations of snow at C-band are sensitive to wet snow due to the high dielectric contrast with non-wet snow surfaces. Synthetic aperture radar (SAR) is now openly available to identify and map the wet snow areas globally at relatively fine spatial resolutions (~100m). In this study, a semi-automated workflow is developed from the change detection thresholding method of Nagler *et al.* (2016) using multi-temporal Sentinel-1A (S1A) dual-polarization observations of Southern Ontario. Regions of Interest (ROIs) were created for agricultural lands to analyze the factors influencing backscatter responses from wet snow. To compare with the thresholding method, logistic regression and Support Vector Machine (SVM) classifications were applied on the datasets. Weather station data and visible-infrared satellite observations were used as ground reference to evaluate the wet snow area estimates. Even though the study merely focused on agricultural land, the results indicated the feasibility of the change detection method with a threshold of -2dB on non-mountainous areas and addressed the usefulness of Sentinel-1A data for wet snow mapping. However, with the capability of identifying non-linear characteristics of the datasets, classification methods tended to be a more accurate method for wet snow mapping. Moreover, this study has suggested using Sentinel-1A data with large incidence for wet snow mapping is feasible.

Acknowledgements

The completion of this thesis would not have been possible without the support and encouragement from many individuals. First and foremost, I would like to express my sincerest gratitude to my supervisor, Dr. Richard Kelly, for his wise mentorship, great patience and continuous support. He always encourages me and spends time guiding me to think independently from different directions. Through this process, I have also learned the wisdom to solve problems. The completion of my master study could not have been accomplished without his endless help and effort. I would also express my appreciation to my committee members: Dr. Christine Dow, Dr. Claude Duguay and Dr. Ellsworth LeDrew. Thanks for providing all the valuable comments and suggestions on my thesis work. I would like to give special thanks to everyone in our research group: Aaron Thompson, Qinghuan Li, Paul Donchenko, Vicky Vanthof, Nastaran Saberi and Margot Flemming. It is my great fortune to have this wonderful group of people supporting and encouraging me. I would like to express my gratitude to all my good friends. I always remember the moments where I gain support and care from you, and thanks for the accompanies. Finally, my most important thanks are to my family. I would like to thank my boyfriend Garry and his parents for accompanying and supporting me during this journey. I would like to thank my dearest parents for their endless love and trust. It was their support and encouragement that helped me get to this point.

Table of Contents

Author's Declaration ii
Abstract iii
Acknowledgements iv
Table of Contents v
List of Figures viii
List of Tables x
Chapter 1 Introduction 1
1.1 Introduction 1
1.2 Goal and Objectives 2
1.3 Thesis Structure 2
Chapter 2 Background: Radar Observations of Wet Snow 4
2.1 Physical properties of snow 4
2.1.1 Snow Formation 4
2.1.2 Snow Cover 4
2.1.3 Snow Metamorphic Processes 5
2.1.4 Phases of Snowmelt 7
2.2 Active Microwave Remote Sensing 7
2.2.1 SAR Basics 7
2.2.2 Radar Equation 9
2.2.3 Polarization 10
2.2.4 Current SAR Systems in Operation 11
2.2.5 Sentinel-1A 13
2.2.6 SAR Image Processing 13
2.3 Radar Remote Sensing for Snow Monitoring 16
2.3.1 Snow Dielectric Properties 16
2.3.2 Snow Backscattering Mechanisms 17

2.3.3 Factors influencing Wet Snow Monitoring 18
2.3.4 Methods on Wet Snow Mapping with SAR 20
Chapter 3 Methodology 23
3.1 Study Area 23
3.2 Data 24
3.2.1 Sentinel -1A Radar Images 24
3.2.2 Meteorological data 25
3.2.3 MODIS Snow Cover Product MOD10L2C 26
3.3 Methodology 26
3.3.1 Preprocessing 26
3.3.2 Calculation of Reference Image 28
3.3.3 Calculation of Ratio Image 28
3.3.4 Regions of Interest (ROIs) Analysis 29
3.3.5 Sensitivity Analysis 30
3.3.6 Evaluation 30
3.3.7 Classification 31
Chapter 4 Results 35
4.1 Standard Thresholding Results 35
4.2 ROI Analysis to Determine Optimum Threshold 39
4.2.1 Ratio 39
4.2.2 Influences from Terrain 40
4.2.3 Relationship between Local Incidence Angle and Ratio 42
4.2.4 Variations of Temperature and Snow Depth 44
4.3 Evaluation of Thresholds for ROIs 46
4.4 Analysis of ROI Classification Results 49
Chapter 5 Discussion 57
5.1 Backscatter Behavior of Wet Snow 57

5.1.1 Terrain 57
5.1.2 Incidence Angle 58
5.1.3 Polarization 59
5.1.4 Meteorological Factors 59
5.2 Threshold Assessment 60
5.2.1 -2dB Threshold 60
5.2.2 Necessity of Adjusting Threshold 61
5.3 Classification 61
5.4 Uncertainties 62
5.4.1 Limited Ground Reference 62
5.4.2 Limited ROIs 63
5.4.3 Residual Speckle Noise 64
5.4.4 Reference Image 64
5.4.5 Imbalanced Data 64
5.4.6 Agricultural Land 60
5.5 Future work 64
5.6 Main Findings 65
Chapter 6 Conclusion 66
References 68
Appendices 74
Appendix A List of Available Sentinel-1A Scenes 74
Appendix B ROI Summary of Ratio Values 78
Appendix C Confusion Matrix for Thresholds 83

List of Figures

Figure 2.1 Vapor movement in destructive metamorphism (McClung & Schaerer, 2006) 6

Figure 2.2 Sintering process in destructive metamorphism (McClung & Schaerer, 2006) 6

Figure 2.3 SAR imaging geometry (Eineder & Bamler, 2014) 8

Figure 2.4 Horizontal and vertical polarizations of a plane electromagnetic wave (Natural Resources Canada, 2018) 11

Figure 2.5 Sentinel 1 Product Levels from Modes (ESA, 2018) 13

Figure 2.6 Potential scattering mechanisms of snow-covered ground, P_t: transmitted signal, P_r: received signal, $\sigma_{g'}$: surface scattering from the ground interface, σ_{gv}: scattering from interactions between ground surface and snow volume, σ_v: volume scattering from the snowpack, σ_{as}: surface scattering at the air-snow interface (Rott *et al.*, 2010) 17

Figure 2.7 Relationship between liquid water content and penetration depth in snow for different frequencies (Ulaby *et al.*, 1984) 19

Figure 3.1 Study Area with Different Image Coverage for Different Time Periods 24

Figure 3.2 Weather Station Map 26

Figure 3.3 Graph Builder Workflow for HH&HV Images 27

Figure 3.4 Graph Builder Workflow for VV&VH Images 27

Figure 3.5 Workflow of Co-registration 27

Figure 3.6 Methodology Workflow 34

Figure 4.1 An example of change detection result from 23:07 UTC, December 16, 2014 (a) is the preprocessed σ^o HH polarized image; (b) is the reference image averaged from images without potential wet snow; (c) is the ratio image calculated from (a) and (b); (d) is the terrain corrected ratio image; (e) is the binary wet snow map from thresholding; (f)-(j) are the results for HV images. 36

Figure 4.2 Binary snow maps of wet snow and NOAA SNODAS SWE maps. Each date (a) - (i), shows: wet snow from the co-polarization data (left); cross-polarized data (middle) with wet snow represented by the black pixels; SNODAS maps of SWE (right). 37

Figure 4.3 Comparisons of Ratio before and after Terrain Correction for 2014-2017 40

Figure 4.4 Local Incidence Angle and Ratio of Wet Snow for (a) HH Polarized Images, (b) HV Polarized Images, (c) VV Polarized Images and (d) VH Polarized Images 42

Figure 4.5 Temperature and snow depth for ratios from VV and VH/HV images. Each pair show the effect of a changing threshold from -2.5 dB to -0.5 dB. (see text for further explanation) 45

Figure 4.6 Plots of Precision and Recall (left) and ROC Curves (right) for logistic regression (a) and SVM (b) classifications of ROIs. 49

Figure 4.7 Changes of Accuracies with Ratio Thresholds 51

Figure 4.8 Distribution of Ratio Values 53

Figure 4.9 Binary Snow Maps from SVM and Logistic Regression 54

List of Tables

Table 2.1 Common bands of SAR systems with frequency and wavelength 8

Table 2.2 Summary of recent and future SAR systems 12

Table 3.1 Potential Wet Snow Days..... 28

Table 3.2 ROI Distribution..... 29

Table 4.1 Average Backscatter before and after Terrain Correction 42

Table 4.2 Accuracy Assessment for Different Thresholds 48

Table 4.3 Classification Accuracies 50

Chapter 1 Introduction

1.1 Introduction

Snow is an important part of the hydrological cycle and contributes to precipitation in many regions above 45° N and S latitudes. As a large storage of frozen freshwater, melting snow can also supply watersheds with ground-water recharge and surface runoff (Bishop *et al.*, 2011). As part of the cryosphere, seasonal snow covers an area of around 46 million square kilometers of the Earth's surface in winter time and plays an important role in the climate system (Dingman, 2015). As a large amount of the sun's energy can be reflected by the bright snow, the surface temperature of the planet is lowered. However, the increase of temperature will result in shrinking of the snow cover and decrease of snow albedo, which will therefore add the absorption of solar radiation and reinforce the increase of temperature. This process is called snow-albedo feedback and demonstrates the positive feedback of shrinking snow cover with increasing temperatures in the climate system (Armstrong & Brun, 2008). By influencing the energy budget between the ground and the atmosphere, changes in snow cover extent can be an indicator for short-term weather and long-term climate changes at both regional and global scales. Studies have shown that snow cover extent has decreased in response to climate change in the Northern Hemisphere (Déry & Brown, 2007; Brown & Mote, 2009; Derksen & Brown, 2012). Thus, it is important to monitor seasonal snow cover changes. Wet snow exists when there is liquid water in the snowpack, and it can be an indicator for the onset of the snowmelt period (Wakahama, 1968). Researchers from the Canadian Sea Ice and Snow Evolution Network (CanSISE) have observed the trend of decrease of the fraction of Canadian land covered by snow from historical datasets with early snowmelt onset, and climate models also project that the snow cover will continue to decrease through 2025 (Mudryk *et al.*, 2017). Therefore, knowledge of the extent of wet snow area can be of great importance for the effective monitoring of climate-induced changes in snowmelt duration and seasonal snowmelt runoff, and it can further provide implications for operational hydrological and ecological applications.

Previous studies used ground-based microwave systems and ground measurements to build physical models to understand the interactions between radar signals and snow (Stiles &Ulaby, 1980). Passive microwave is suitable for near-daily dry snow mapping and estimation of snow water equivalent (SWE). However, the spatial resolution is coarse, typically at 25 x 25 km^2

(Rott&Nagler, 1994). Synthetic aperture radar (SAR), which is an active microwave system, can provide data at relatively fine spatial resolutions and is able to detect wet snow (Nagler *et al.*, 2016). With the launch of spaceborne active microwave remote sensing systems, satellite radar images have become a useful tool to observe seasonal snow cover under all-weather conditions with repeat passes for regional and global scale imaging at fine spatial resolutions (Nagler&Rott, 2000). C-band has been shown to be sensitive to wet snow as wet snow has an explicit reflection characteristic under C-band due to the high dielectric contrast with non-wet snow surfaces. While dry snow is generally transparent to C-band, C-band is able to identify wet snow for an area pre-identified as snow. As C-band SAR datasets become openly available with multi-temporal imaging producing frequent revisit intervals, they provide an opportunity to map wet snow within an operational context. Studies have demonstrated change detection methods to identify wet snow with single-polarized C-band SAR satellites such as ERS-1/2 and RADARSAT (Baghdadi *et al.*, 1997; Magagi &Bernier, 2003). With the availability of dual-polarized SAR observations, Nagler and other researchers (2016) have improved the method to enable a more accurate monitoring of wet snow. The method has been tested to be robust in mountainous areas, but very few studies have applied the method to detect wet snow in non-mountainous areas, especially areas with various land cover.

1.2 Goal and Objectives

Given the importance of wet snow mapping and the lack of applications in non-mountainous areas, this study aims to assess the applicability of change detection method and a conventional threshold (Nagler *et al.*, 2016) for wet snow mapping in Southern Ontario by using Sentinel-1A (S1A) C-band SAR dual-polarized observations. To achieve the main goal, the following objectives are set:

1) To understand the factors influencing backscatter behaviors of wet snow;
2) To evaluate the conventional threshold of -2dB;
3) To explore new wet snow detection method for Southern Ontario.

1.3 Thesis Structure

The remainder of this thesis is organized into the following chapters. Chapter 2 provides background information of snow processes and SAR imaging. It also describes the interactions between snow and radar. Moreover, it includes a review of the applications of SAR on snow

mapping. Chapter 3 implements the change detection method on the study area and demonstrates the detailed processes for evaluation of the results. Classification methods are also presented. Chapter 4 provides the results of the proposed method. Chapter 5 explains the different cases to understand the factors influencing backscatter and discusses the performance of the different methods. Uncertainties of the study is also discussed. Finally, Chapter 6 summarizes the study with main findings and provides ideas for future work.

Chapter 2 Background: Radar Observations of Wet Snow

2.1 Physical properties of snow

Snowfall forms from atmospheric water vapor through a complex process. The structure of snow undergoes huge microstructure changes from the time when the snow falls through the atmosphere through its lifetime during accumulation on the ground (Armstrong & Burn, 2008). A snowpack also undergoes a series of microstructural changes during the snowmelt period. To help further explain the interactions between snow and radar, it is important to understand the processes of formation and results in physical properties of snow.

2.1.1 Snow Formation

When the air temperature is below the freezing point and the air is supersaturated (humidity exceeds 100 %), water molecules attach and freeze to a tiny dust grain, and form an ice nucleus in the atmosphere (Kumai, 1961). With more water molecules condensing through sublimation, snow crystals grow from ice crystals, which originate from the ice nuclei through nucleation (Libbrecht, 2005). As the air temperature and humidity varies, snow crystals will grow into different shapes, structures and sizes. When snow crystals aggregate, a snowflake is formed. Then, as snow falls to the ground, a new snow layer may be aggregated. When snow layers accumulate, a snowpack can be built up over time. As a porous medium, the microstructure of a snowpack consists of a continuous ice structure and connected pore spaces with air and liquid content. When the temperature of snow is below 0℃, there is only air in the pore spaces; when snow starts to melt or it rains, the liquid water begins to fill in the pores.

2.1.2 Snow Cover

Snow cover describes the extent of ground covered by snow. Variations in local environmental conditions create differences spatially and temporally in snow cover accumulation characteristics. Temperature is a driving factor that can greatly influence the basic formation of snow and the rate for snow melt, thereby influencing the extent and depth of snow cover (Teubner *et al.*, 2015). Wind redistributes snow crystals and changes their properties in the process, thereby altering the density and surface roughness of a snowpack (Gray *et al.*, 1971). Geomorphologic features, such as elevation and slope can dominate snow cover patterns (Meiman, 1970). In addition to these factors, vegetation cover can also influence the snow transportation and accumulation (Hall *et al.*, 1998).

For example, researchers simulated a low-Arctic catchment with different shrub coverage, which indicated that the snow depth increases with higher shrubs of shrub-covered areas (Essery & Pomeroy, 2004). All these factors do not function alone, but can be related to each other and change snow cover distribution characteristics through a complex process with energy transfer.

2.1.3 Snow Metamorphic Processes

Continuous changes in the snowpack structure occur under a series of metamorphism processes when the snow becomes isothermal close to its melting point. Metamorphism refers to the processes that snow grains change in size, shape and cohesion, which are driven by thermal conditions (Armstrong & Brun, 2008). Throughout the time that the snow deposits on the ground until it melts, there will be a vertical temperature gradient from the surface to the inside of the snowpack due to the vapor and heat exchange (Sturm *et al.*, 2002). As a result of the temperature gradient, there are three main different types of metamorphism cited, called destructive, constructive and melt metamorphism. The former two occur in the dry snow pack and the last one in the wet snow.

2.1.3.1 Destructive Metamorphism

When there is a small temperature difference from the top to the bottom of the snowpack (<10℃ m^{-1}), destructive metamorphism dominates the dynamical process (Sommerfeld & LaChapelle, 1970). Because the vapor pressure over the curved surface increases with the decrease of the radius, the point parts of the snow crystals are under high vapor pressure. Therefore, sublimation will occur on these convex surfaces, whereas the water vapor will move moisture to the concave areas to deposit as ice and gradually fill the hollow (Figure 2.1). Through this process, the snow grains become rounded, and the density also increases during this period (Colbeck, 1983). When the round snow grains touch each other, they will be sintered with a neck, which raise the strength of the snow pack (Figure 2.2).

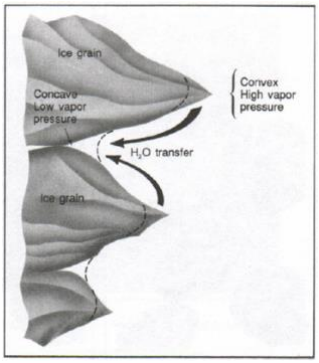

Figure 2.1 Vapor movement in destructive metamorphism (McClung & Schaerer, 2006)

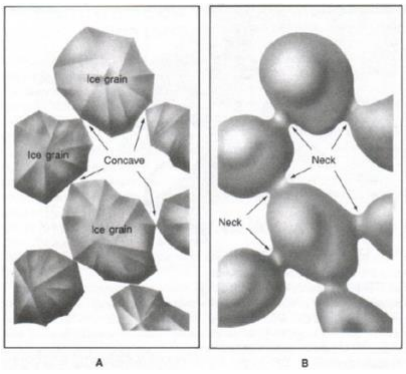

Figure 2.2 Sintering process in destructive metamorphism (McClung & Schaerer, 2006)

2.1.3.2 Constructive Metamorphism

When a larger temperature gradient (>=10℃ m^{-1}), the snowpack typically undergoes constructive metamorphism (McClung & Schaerer, 2006). As the sub-nivean soil supplies the heat, and the snow layer helps to retain the heat, the bottom of the snow pack is warmer than the upper parts. Because of the temperature gradient, there is a vapor gradient forming in the snowpack, and the pressure of water vapor is higher at the bottom than at the top. Therefore, sublimation occurs at the bottom due to supersaturation, and the water vapor moves upward. The water vapors then condense and deposit at the cold snow grains, and the rounded grains will become faceted (Colbeck, 1983). With a large temperature gradient, depth hoar will form, which is a cup-shaped grain that loosely bond with each other (Akitaya, 1974).

2.1.3.3 Melt Metamorphism

Melt metamorphism occurs at the beginning and the end of the snow season. Liquid water usually exists when the snow starts to melt at the surface or it rains. Because of the force of gravity, the surface water molecules descend into the snow pack, and refreeze in the middle layers. As the

refreezing releases some energy, it warms the snowpack and increase the vapor transfer (Colbeck, 1973). Moreover, the rounded grains will aggregate into larger grains around 1 to 2 mm, whereas the smaller snow grains will disappear. Therefore, the density of snowpack will increase.

2.1.4 Phases of Snowmelt

The snow melt processes usually undergo three main phases with continuous net energy inputs (Dingman, 2015). The first phase is the warming phase when there is no melt, but the snowpack is warmed to a stage when the snowpack is isothermal at 0 ℃. When the temperature no longer changes, and the energy input will result in the melting of ice to melt water, the ripening phase will start. The meltwater remain in the pore spaces until the snowpack is unable to retain water, and the ripening phase will finish. The water can be retained because of the surface-tension, which is able to work against the gravity force during the ripening phase (Shelton, 2009). The last phase, which is called output phase, will start when the snowpack is ripe and the pores can no longer hold the water; meltwater starts to percolate from the snowpack. Thus, the snowpack will continuously absorb energy and the process will cause water output (Etchevers *et al.*, 2004).

2.2 Active Microwave Remote Sensing

As it is important to monitor the seasonal snow cover changes, microwave remote sensing systems is a useful tool to observe ground features without the influence from weather, especially clouds.

There are two main types of microwave remote sensing systems: active and passive microwave. While passive microwave systems receive the radiation emitted from the surface at coarse spatial resolutions (>100 km^2), active microwave systems can transmit specific frequencies of microwave energy and receive the returned signal at spatial resolutions of <400 m^2 (Royer, 2010). Synthetic aperture radar (SAR) is an active microwave sensing system that can observe a wide range of land and ocean surfaces and can differentiate features based on the measured backscatter signal.

2.2.1 SAR Basics

SAR, usually mounted on an airborne or space borne platforms, is a side-looking microwave radar system that generates high resolution two dimensional (2-D) images (Ulaby et al, 2014). The commonly used range of microwave for SAR system is between Ka-band to P-band (Table 2.1). A SAR system involves a pulsed microwave transmitter, an antenna and a receiver unit. For a

monostatic SAR system, the antenna is capable of transmitting the microwave pulses into beam towards the ground and also obtaining the echoes of the signal reflected from the ground. The backscatter signal strength of a target is often measured as backscattering cross section (σ), which is the scattering cross section in the direction toward SAR. The location of the target can be calculated from the distance between the target and sensor by obtaining the time delay between the signal transmission and reception (Moreira, 2013).

Table 2.1 Common bands of SAR systems with frequency and wavelength

Band	**Ka**	**Ku**	**X**	**C**	**S**	**L**	**P**
Frequency (GHz)	40-25	17.6-12	12-7.5	7.5-3.75	3.75-2	2-1	0.5-0.25
Wavelength (cm)	0.75-1.2	1.7-2.5	2.5-4	4-8	8-15	15-30	60-120

A typical SAR side looking geometry is illustrated in Figure 2.3. Azimuth refers to the flight direction, whereas ground range is perpendicular to the flight direction. The beam from the antenna transmit towards the ground with an incidence angle θ. Slant range is the distance between the SAR sensor and the target, while the ground range is the horizontal distance from the target on the ground to the nadir track. The ground area covered by the beam is called the antenna footprint. When the SAR is moving along the flight direction, the scanned area is the radar swath. The part of swath that is closest to the nadir track is the near range, and the farthest part is the far range.

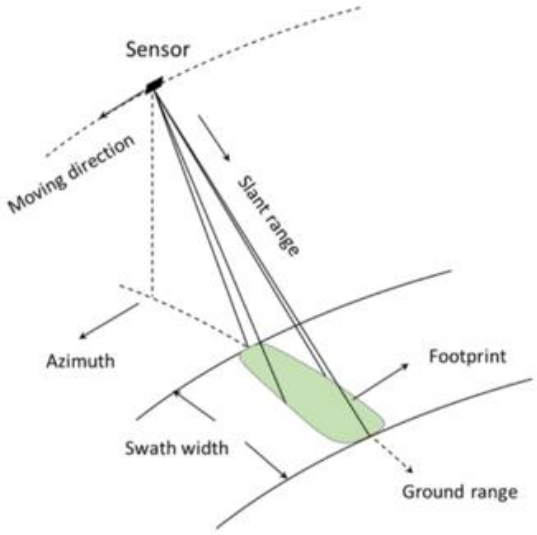

Figure 2.3 SAR imaging geometry (Eineder & Bamler, 2014)

Spatial resolution refers to the ability to distinguish two closely spaced objects, and the resolution for SAR can be determined in range and azimuth direction. The sensor can differentiate targets in slant range direction when the time difference of echoes is larger than the effective pulse propagation time. Therefore, slant range resolution is a fixed value that is dependent on the pulse length. As the horizontal expression of slant range resolution, ground range resolution is a function of slant range resolution and incidence angle. Because incidence angles are different from near to far range, ground range resolution changes across the footprint (Richards, 2009). On the other hand, azimuth resolution is calculated by the length of antenna and radar wavelength. Since longer antenna will result in narrower beam and finer azimuth resolution, SAR achieves this goal by synthesizing the effective length of antenna. In general, range resolution and azimuth resolution are independent to the height of the sensor above ground level.

2.2.2 Radar Equation

The radar equation estimates the power returned to the radar sensor from a target with known radar cross section at a specific range (Woodhouse, 2006). Because energy propagates in a spherical pattern, the power density at the target can be calculated with the total transmitted power P_t (Watt) divided by the surface area of the sphere with the radius R (meter). Due to the directional beam pattern of the antenna, the incident power density Q_i (W/m^2) will increase with a transmit antenna gain factor G_t:

$$Q_i = \frac{P_t G_t}{4\pi R^2} \tag{2.1}$$

The power reflected by the target towards the radar system $P_{reflect}$ (W) is the product of the incident power density and the radar cross section σ (m^2) of the target:

$$P_{refelct} = Q_i \sigma = \frac{P_t G_t \sigma}{4\pi R^2} \tag{2.2}$$

The radar cross section σ characterizes the target's reflected response, and is a measure of the ratio between backscatter density in the direction towards the receiver and the power density intercepted by the target. Physical features of the target such as the material and size, parameters of the radar system such as the frequency and direction can influence the radar cross section. The power density at a receive antenna Q_r (W/m^2) is the reflected power divided by the spherical area:

$$Q_r = \frac{\mathrm{P_{reflect}}}{4\pi \mathrm{R}^2} = \frac{\mathrm{P_t G_t \sigma}}{(4\pi)^2 \mathrm{R}^4} \tag{2.3}$$

The power measured by a radar receive antenna P_r (W) with an effective antenna area of A_e (m^2) can be expressed as:

$$P_r = Q_r A_e = \frac{P_t G_t A_e \sigma}{(4\pi)^2 R^4} \tag{2.4}$$

The effective aperture area A_e (m^2) is related to the wavelength of radar λ and the receive antenna gain G_r, which can be represented as:

$$A_e = \frac{\lambda^2 G_r}{4\pi} \tag{2.5}$$

In a monostatic radar system, the receiver and transmitter antenna are the same and have the same gain factor. Therefore, the power P_r (W) is given by:

$$P_r = \frac{P_t G_t G_r \lambda^2 \sigma}{(4\pi)^3 R^4} = \frac{P_t G^2 \lambda^2 \sigma}{(4\pi)^3 R^4} \tag{2.6}$$

The normalized radar cross-section σ^o, which comes from normalizing the radar cross section by the illuminated area (A), provides the capability to compare and characterize the backscatter of a target from different instruments. From Equation 2.6, σ^o can be solved as:

$$\sigma^o = \frac{\sigma}{A} = \frac{P_r (4\pi)^3 R^4}{P_t G^2 \lambda^2 A} \tag{2.7}$$

2.2.3 Polarization

For a plane electromagnetic wave, polarization is the orientation of the electric field vector against the horizontal direction (Woodhouse, 2005). If the orientation is along the horizontal direction, the wave is horizontally polarized (indicated as H); when it is perpendicular to the horizontal direction, the wave is vertically polarized (indicated as V) (Figure 2.4). SAR systems are capable of detecting the polarization of the backscattered signals, and based on the polarization types that the sensor transmits and receives, there are four polarization configurations: HH, HV, VV and VH. A single-pol system (HH or VV) transmits H or V waves and receives the same polarization. A dual-pol system (HH and HV or VV and VH) usually transmits waves in H or V polarization and receives both. A quad-pol or full-pol system (HH, HV, VH and VV) can transmit both H and V waves and measures both H and V when receiving. While the majority of SAR systems are linearly polarized, it is also possible to create non-linear polarizations such as circular polarization.

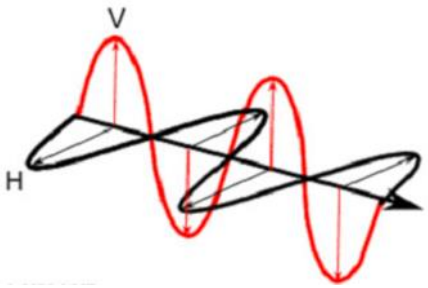

Figure 2.4 Horizontal and vertical polarizations of a plane electromagnetic wave (Natural Resources Canada, 2018)

2.2.4 Current SAR Systems in Operation

Since the launch of the first civilian SAR satellite Seasat in 1978, SAR has been widely used to observe the detailed features of the Earth surface with high resolution images. In the 1990s, SAR techniques were greatly developed to improve the retrieval of Earth surface parameters and information, such as polarimetry and interferometry. With the development of satellite SAR observing systems, more frequent repeated pass products have provided increased potential to monitor the Earth surface changes through multi-temporal images. The major SAR satellites in operation currently are low frequency, which are suitable for wet snow detection. Recent and future SAR sensors are summarized in Table 2.2.

Table 2.2 Summary of recent and future SAR systems

Sensor	Year	Country	Institute	Frequency	Polarization
Seasat	1978	USA	NASA/JPL	L	HH
ERS-1 ERS-2	1991-2000 1995-2011	Europe	ESA	C	VV
SIR-C/X-SAR	1994	USA, Germany Italy	NASA DARA ASI	L& C X	HH, HV, VV, VH VV
RADARSAT-1	1995-present	Canada	CSA	C	HH
SRTM	2000	USA, Germany Italy	NASA DARA ASI	C X	HH VV
ENVISAT/ASAR	2002-2012	Europe	ESA	C	HH/VV, HH/HV, VV/VH
ALOS/PalSAR	2006-2011	Japan	JAXA	L	HH, HV, VV, VH
TerraSAR-X TanDEM-X	2007-present 2010-present	Germany	DLR EADS Astrium	X	HH, HV, VV, VH
RADARSAT-2	2007-presnet	Canada	CSA	C	HH, HV, VV, VH
COSMO-Skymed-1/4	2007-prensent 2010-presnet	Italy	ASI	X	HH&VV, HH&HV, VV&VH
RISAT-1	2012-present	India	ISRO	C	HH, HV, VV, VH
HJ-1C	2012-present	China	CAS	S	VV
KOMPSAT-5	2013-present	Korea	KARI	X	HH&VV, HH&HV, VV&VH
Sentinel-1A/1B	2013-present 2015-present	Europe	ESA	C	HH&VV, HH&HV, VV&VH
ALOS-2 PALSAR-2	2014-	Japan	JAXA	L	HH, HV, VV, VH
Gaofen-3	2016-present	China	CAS	C	HH, HV, VV, VH
RADARSAT Constellation	2018	Canada	CSA	C	HH, HV, VV, VH

2.2.5 Sentinel-1A

The Sentinel missions, as part of the Copernicus program undertaken by the European Space Agency (ESA), include a series of radar and optical satellites that undertake observations of the Earth surface. Sentinel-1 is a C-band SAR satellite constellation that consists of two satellites. Sentinel-1A, which was launched in April 2014, started providing imagery in October 2014, and Sentinel-1B, which was launched in April 2016, and started providing imagery more recently. Sentinel-1A provides an exact revisit period of 12 days, and a revisit of 6 days can be achieved with Sentinel-1B. Sentinel 1 offers four acquisition modes: Stripmap (SM), Interferometric Wide swath (IW), Extra-Wide swath (EW) and Wave (WV). SM, IW and EW are available with both single polarization (HH/VV) or dual polarization(VV+VH/HH+HV), while WV data is only with single polarization. Images acquired from IW and EW modes have large swath of 250km (IW) and 400km (EW) by virtue of using Terrain Observation with Progressive Scans SAR (TOPSAR) technique. TOPSAR is capable of reducing the scalloping effect by steering the beam both in the azimuth and range direction, and it can therefore obtain more homogeneous image quality than traditional ScanSAR mode (De Zan & Guarnieri, 2006). The data from Sentinel-1 are provided in three processing levels: Level-0 data refers to the raw data signal, Level-1 data can be Single Look Complex (SLC) or Ground Range Detected (GRD) and Level-2 data is Ocean (OCN). Figure 2.5 shows the available products from the four modes. With open and free access to Sentinel-1 data, the large user community have demonstrated wide applications of Sentinel 1 products.

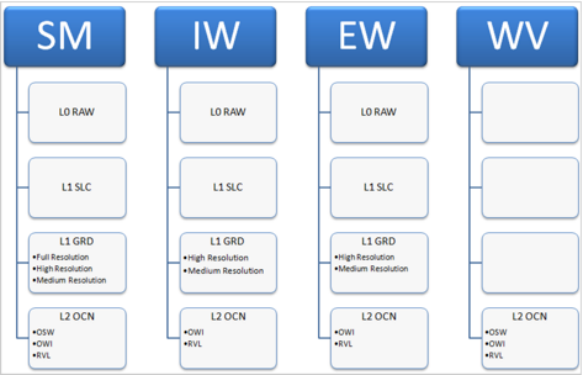

Figure 2.5 Sentinel 1 Product Levels from Modes (ESA, 2018)

2.2.6 SAR Image Processing

The raw data signals received by SAR sensor are in the form of complex number with a real part and an imaginary part. Single look complex (SLC) images, which are the first level images

transformed from the raw signals, can be obtained through a process called focusing. The focusing process aims to gather the energy spread from range and azimuth into a single pixel. There are several steps contributing to this process, they are: Doppler centroid estimation, range compression, range migration and azimuth compression (ESA, 2017). SLC images can be used for quality assessment, calibration and can provide phase information.

For each pixel in SLC image, it does not only contain the amount of backscatter power received, but also stores the microwave phase information, so each pixel value in SLC images is in a complex form. A process named detection converts the complex value into a digital number, so that the image can be interpreted by human eyes. Intensity, also called power, can be calculated from the complex values as:

$$Intensity/Power_j = (I_j\ )^2 + (Q_j\ )^2 \tag{2.8}$$

where I_j is the in-phase part (stored as the real part of the complex storage number), and Q_j is the quadrature (imaginary part of the complex number) of j^{th} pixel from the start of the range line.

Amplitude, which is the square root of intensity, is often used as the digital number (DN). DN_j is the digital number for the j^{th} pixel, and it can be calculated as:

$$DN_j = \sqrt{(I_j\ )^2 + (Q_j\ )^2} \tag{2.9}$$

Due to the interference of electromagnetic waves scattered from the ground and objects, SLC data has maximum speckle noise. Multi-looking is a common first-step to reduce speckling by averaging the values among the pixels. SLC image data usually look narrow because each pixel is rectangular in shape. Multi-looking combines N pixels into an approximately squared pixel, where N is called the number of looks. Therefore, the number of looks is related to pixel spacing in azimuth, pixel spacing in slant range and the look angle at scene center, and it can be calculated as follows:

$$number\ of\ looks\ \approx\ \frac{ground\ range\ resolution}{pixel\ spaing\ in\ azimuth}$$

$$= \frac{pixel\ spacing\ in\ azimuth/\sin(incidence\ angle)}{pixel\ spacing\ in\ azimuth} \tag{2.10}$$

Ground Range Detected (GRD) images are the next level product based on SLC data which have been detected, multi-looked and converted to a ground range projection using an Earth ellipsoid

model such as WGS84. The GRD data still needs further processing to reduce speckle and apply a geo-referencing and radiometric calibration.

Speckle filters are applied to reduce the speckle noise remaining after multi-looking. Speckle noise is multiplicative and so adaptive filter functions based on the statistics calculated for each pixel and the surrounding pixels can retain edge features and image texture in a heterogeneous area and preserve radiometric information for a homogeneous area (Lopes *et al.*, 1990). Kuan and Lee filters smooth the speckle by minimizing the mean squared error in the fixed window (Ko & Lee, 1991). The Frost filter computes the un-speckled value for each pixel from the weighted sum of the values through a convolutional process in a fixed window (Frost *et al.*, 1982). The Gamma filter is a maximizing à posteriori (MAP) filter that assumes the data are gamma distributed and calculate the pixel values based on Bayesian analysis (Baraldi & Parmiggiani, 1995). Filter kernel sizes can greatly influence the results; too large a filter can result in loss of details while too small a filter might not be effective to reduce speckle (Yu & Acton, 2002). However, speckle noise inherently exists in the radar images and cannot be completely removed even after applying multi-looking and speckle filters, which can add more uncertainties when interpreting the SAR images on a pixel basis.

Radiometric calibration is critical to standardize the backscatter information and make features in different images acquired from different sensors comparable. Look Up Tables (LUTs), which calculate the backscatter values with a range-dependent gain, are usually contained in the downloaded product folder as the calibration annotation dataset. Radar brightness coefficient (β^0) is the reflectivity in slant range geometry, and can be calculated as:

$$\beta_j^0 = (DN_j^2)/A2_j \tag{2.11}$$

DN_j refers to the digital number for the j^{th} pixel from the start of a range line in a detected image, $A2_j$ is the scaling gain value for the j^{th} pixel. Radar brightness coefficient in dB can be calculated as:

$$\beta_j^0(dB) = 10 * log_{10}[(DN_j^2)/A2_j] \tag{2.12}$$

Radar backscatter coefficient (σ^0) refers to the strength of radar signals for a pixel, and can be calculated as:

$$\sigma_j^0 = \beta_j^0 * (sin\theta_j) \tag{2.13}$$

Θ_j is the incidence angle at j^{th} pixel. The backscatter coefficient in decibel can be calculated as:

$$\sigma_j^0(dB) = \beta_j^0(dB) + 10 * log_{10}(sin\theta_j) \quad (2.14)$$

To identify the coordinate system and reduce the distortion of the image, geocoding converts the slant-range or azimuth geometry to a map projection. Using a Digital Elevation Model (DEM), the correction process is called Terrain Geocoding, whereas Ellipsoidal Geocoding refers to the process without a DEM. Then, the pixels from SAR images should be resampled to the according coordinate system (ESA, 2017).

2.3 Radar Remote Sensing for Snow Monitoring

SAR can provide images at relative fine spatial resolutions without the influence of weather conditions, especially at C-band or lower frequencies. Therefore, it provides an opportunity to monitor terrestrial snow cover changes. As the snow structures can change over time, it is important to understand the physical interactions between snow and radar signals. Previous research using SAR for snow monitoring provides further insight for this thesis.

2.3.1 Snow Dielectric Properties

Snow is a dielectric material that cannot easily conduct electric current, and its dielectric properties influence its response to microwave. The dielectric constant, also known as relative permittivity, is used to quantify a material's electromagnetic propagation properties (Woodhouse, 2005). The dielectric constant at 0 °C for air is 1, pure ice is 3.15 and water is 80 (Hallikainen, 1977). As the dielectric constant of water and ice are extremely different, the dielectric properties of snow are generally dominant by the amount of water in a snowpack with the same volume under a given microwave frequency (Ulaby *et al.*, 1977). Dry snow is composed by ice and air, whereas wet snow is a mix of ice, air and liquid water in ripening and output phases; therefore, dry snow and wet snow have different responses to microwave (Evans, 1965; Ulaby & Stiles, 1981). As liquid water will cause high dielectric loss so that the snowpack will emit more microwave energy, the penetration depth of microwaves will decrease (Rott *et al.* 1988; Shi & Dozier, 1997). It was found that when the snowpack gets wet around 4-5% liquid water content, the penetration depth of radar signal will decrease to 3-4 cm (Mätzler and Schanda, 1984). Moreover, the physical properties of snowpack, such as snow density, grain size and temperature can also influence the snow's dielectric properties (Chang *et al.*, 1982; Rosenfeld 2000). Ulaby and Stiles (1981)

concluded that "the dielectric constant of snow is a function of frequency, snow wetness, temperature and density, among other less influential parameters".

2.3.2 Snow Backscattering Mechanisms

Generally, the frequency-dependent backscatter of a snowpack generates from two scattering types, which are surface and volume scattering. Surface scattering can occur at the snow-ground interface, interfaces between snow layers and the air-snow interface. Volume scattering occurs within the snowpack, where the signals interact with ice crystals in an air background (Ulaby *et al.*, 1984). Rott *et al.* (2010) summarized the total backscatter of a snowpack as:

$$\sigma_t = \sigma_{g'} + \sigma_{gv} + \sigma_v + \sigma_{as} \tag{2.15}$$

where $\sigma_{g'}$ is the surface scattering from the ground interface, σ_{gv} is the scattering from interactions between ground surface and snow volume, σ_v is the volume scattering from the snowpack, and σ_{as} is the surface scattering at the air-snow interface (Figure 2.6).

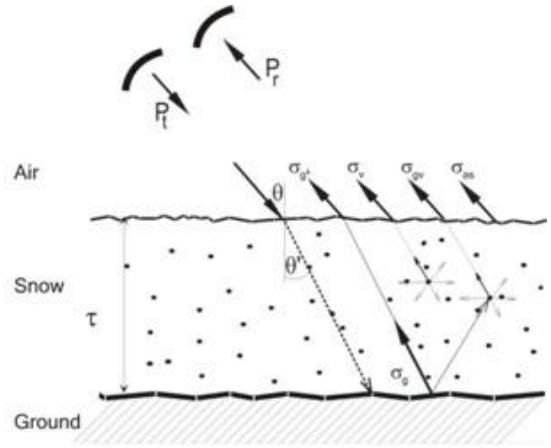

Figure 2.6 Potential scattering mechanisms of snow-covered ground, P_t: transmitted signal, P_r: received signal, $\sigma_{g'}$: surface scattering from the ground interface, σ_{gv}: scattering from interactions between ground surface and snow volume, σ_v: volume scattering from the snowpack, σ_{as}: surface scattering at the air-snow interface (Rott *et al.*, 2010)

For a snowpack, because the penetration depth is based on the frequency of microwave, the interactions of scattering mechanism are different for different frequencies. As C-band can usually penetrate through a seasonal dry snowpack, there is no scattering interaction with the snowpack, and the scattering will mainly come from the ground. At shorter wavelengths such as Ku-band, different types of scattering will occur in a dry snowpack. Ground surface scattering and volume

scattering will dominate because the surface scattering from the air-snow interface and interfaces of snow layers can be ignored due to low dielectric contrast between the boundaries. Therefore, parameters such as snow density, snow grain size, snow water equivalent and ground properties can influence the backscatter characteristics of dry snow. On the other hand, where the snow is wet, there is a decrease of the penetration depth of C-band and the backscatter comes from surface scattering of air-snow interface and volume scattering. Thus, snow properties such as surface roughness and liquid water content can influence the frequency-dependent scattering strength (Shi *et al.*, 1995). The surface scattering will increase with rougher wet snow surface, while volume scattering will dominate when the wet snow surface is smooth (Guneriussen, 1998).

2.3.3 Factors influencing Wet Snow Monitoring

The backscatter of a snowpack will behave differently under different parameters of a SAR system, so it is important to find optimal conditions of datasets for wet snow mapping. Frequency, polarization and incidence angle of a SAR system are three key factors for identifying wet snow. By understanding the factors, researchers will be able to use the suitable datasets.

2.3.3.1 Frequency

At specific frequencies, microwaves can penetrate part of a dry snowpack without any absorption of energy, but the penetration depth is decreased when the liquid water content increases. The penetration depth δp (m) of a wave in snow is dependent on λ and the real and imaginary portions of the relative permittivity ε' and ε" of snow:

$$\delta_p = \frac{\lambda\sqrt{\varepsilon\prime}}{2\pi\varepsilon''} \tag{2.16}$$

Figure 2.7 presents the relationship between penetration depth and snow liquid water content for different frequencies. Therefore, it is possible to discriminate wet snow from dry snow assuming snow is present. Different microwave frequencies show different sensitivities to snow wetness, and studies have found that C-band is very sensitive to wet snow and can penetrate through a seasonal dry snowpack (Matzler & Schanda, 1984). Therefore, dry snow is generally transparent under C-band and can hardly show differences from bare ground, while wet snow has an explicit reflection characteristic due to the high dielectric contrast with non-wet snow surfaces. C-band is an excellent microwave frequency to identify wet snow (Rott & Nagler, 1993).

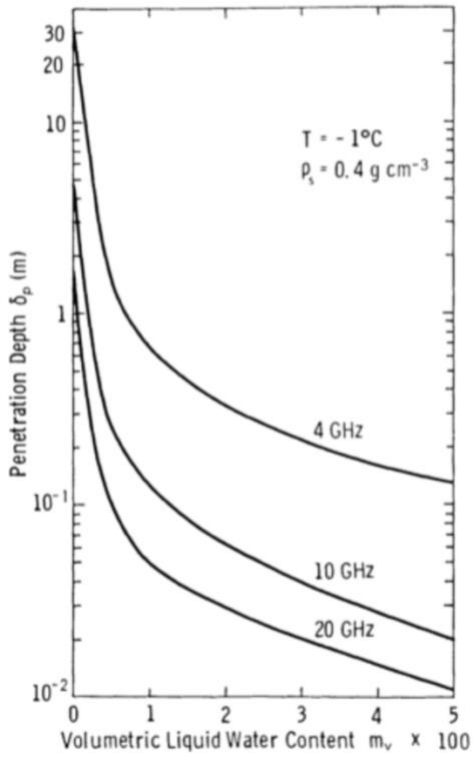

Figure 2.7 Relationship between liquid water content and penetration depth in snow for different frequencies (Ulaby *et al.*, 1984)

2.3.3.2 Incidence angle

The influence of incidence angle of the SAR observation on the backscatter from wet snow covered surface and non-wet snow surface can be significant. Generally, surface scattering dominates the backscatter at near-nadir incidence angles, while at large incidence angles, backscatter mainly consists of volume scattering (Ulaby *et al.*, 1986). Matzler and Schanda (1984) found that backscatter of 10.4 GHz (X-band) at incidence angles greater than 20° can differentiate wet snow from dry snow. Baghdadi *et al.* (1998) explored the relationship between incidence angles and C-band HH, VV and VH polarizations when identifying different land surface types covered by wet snow, and found that incidence angles over 30° have fewer influences on the classification results. Guneriussen *et al.* (2000) concluded that wet snow and bare ground showed more distinct differences at large incidence angle (45°) of RADARSAT S7 mode (C-band) than the differences at lower incidence angle (24°) of S2 mode. Magagi and Bernier (2003) suggested that RADARSAT S7 mode, which has a range of incidence angle from 45 to 49°, is more suitable to map wet snow than S1 mode which is in low incidence angles from 20 to 27°.

2.3.3.3 Polarization

Early studies on wet snow mapping (Bernier *et al.*, 1994; Baghdadi *et al.*, 1998) mainly focused on single co-polarization data (HH/VV) due to the availability, and with accessibilities of dual-polarized and full-polarized images, the results showed higher accuracies (Park *et al.*, 2014; Nagler *et al.*, 2016). Ulaby *et al.* (2004) concluded that the influences from incidence angle on the contrast of backscatter between wet snow and non-wet snow surfaces are different under co-polarization and cross-polarization. For co-polarized images, low incidence angles will result in a less clear difference of backscatter; while for cross-polarized images, the differences remain clear. On the other hand, at high incidence angles, cross-polarized backscatter would be noisy. Therefore, a combination of cross- and co-polarization images should be used to identify wet snow (Nagler *et al.*, 2016).

2.3.4 Methods on Wet Snow Mapping with SAR

Early studies of wet snow mapping were based on backscatter models and experimental tests of aircraft SAR system with multiple frequencies (Bernier, 1987). As SAR satellite systems start providing repeated pass products, multi-temporal images are involved and enable frequent monitoring of wet snow. A change detection method by using the image ratio to compare two images pixel by pixel has been developed based on the low backscatter of wet snow compared to dry snow for wet snow mapping with C-band SAR images by Rott and Nagler (1993). The change detection method first calculates the ratio between images with snow and without snow for the same study area, and then applied a threshold of -3 dB to map wet snow areas with values less than -3 dB. Although only single polarization images were used, by involving multi-temporal images, the accuracy of wet snow identification has been greatly improved. Other studies have developed based on this basic method but modified this method for better classification results under different environmental conditions. Baghdadi *et al.* (1997) added minimum and maximum range for wet snow backscatter coefficients to improve the classification accuracy. Nagler and Rott (2000) improved the original method for a mountainous area by using the average value of several reference images to reduce the environmental influences on backscattering, combining ascending and descending images to reduce layover effects and masking out the layover and shadow areas to refine misclassifications. The study also suggested that RADARSAT S7 mode is more suitable than S1 mode for wet snow mapping in mountainous terrain because of the great influences of

small incidence angles on co-polarization. With the availability of multi-polarized images, researchers have improved wet snow detection methods and combined the co- and cross-polarizations to reduce the influences from incidence angle. Nagler *et al.* (2016) applied the change detection method on Sentinel-1A dual polarization (VV VH) images with a -2dB threshold, and combined the ratio images calculated from the two polarization modes with a weighted function into a single channel based on the local incidence angle. Because the study area is in a mountainous region, layover mask and radar shadows were generated to refine the results. Instead of using a fixed threshold, Besic *et al.* (2015) added a stochastic process to identify the probability for wet snow. Rondeau-Genesse *et al.* (2016) generated a formula based on the Nagler's change detection method to calculate the probability of wet snow in a basin area, and this method was able to identify the wet snow areas with low liquid water content and influenced by forest cover. Because of the visualization of snow cover, visible-infrared images are often used to refine and validate the classification results when available. Additionally, some studies (Haefner & Piesbergen, 1997; Solberg et al, 2004) used a data fusion method to combine the optical and SAR images pixel by pixel to map the snow-covered areas.

The various methods described above mainly used single or dual polarized images, while with accessibilities of full polarimetric data, researchers developed more robust methods based on the variations of the physical parameters among the different snow types from decompositions. Supervised classification such as Support Vector Machine (SVM) methods are used to classify the wet snow-covered areas with the polarimetric features (Huang *et al.*, 2011; Park *et al.*, 2014). SVM is commonly used because of its capability of solving non-linear problems with limited samples. He et al. (2015) applied a SVM classifier based on the training samples generated from the polarimetric parameters and in situ datasets to identify the snow cover changes and resulted in a high accuracy of 90%.

In summary, wet snow mapping methods have improved as more frequent and accessible data have become available. The change detection method of Nagler and Rott (2016) has been proven to be robust for mountainous area, while it has not been widely tested in non-mountainous areas. Moreover, a common threshold of -2dB was used for several studies, however, the threshold might be different based on the local statistics of the study area. Studies have observed the differences between wet snow and non-wet snow can vary due to the local incidence angles and surface

properties of snow (Guneriussen, 1997). Therefore, it is important to assess the applicability of the method to different study areas, especially areas with complicated conditions.

Chapter 3 Methodology

3.1 Study Area

The study area is located within Southern Ontario, Canada (around 42~44°N, 79~83°W). As the most populated area in Ontario, Southern Ontario has well-built infrastructure and developed industries. Apart from the urban areas, agricultural and natural lands cover the majority of the region. The elevation for the study area is relatively flat, while the highest areas are located near Dufferin and western of Simcoe counties. Because of the Niagara Escarpment, there are limestone cliffs from the Niagara peninsula running northwest to the Bruce Peninsula from Niagara (Ontario Ministry of Natural Resources, 2018). There is abundant freshwater storage from the Great Lakes, watercourses and inner lakes within this region. With a continental climate, Southern Ontario's weather is tempered the Great Lakes, which generally promotes warmer temperatures than the other parts of Ontario (Teskey, 2012). During the winter, this region typically undergoes a long period of 6 months (November-April) with heavy snowfall. The average annual snowfall can vary from south to north around 120-200 cm from south to north (Environment Canada, 2010). Sturm and Holmgren (1995) classified the seasonal snow cover of Southern Ontario as maritime snow, which has frequent snowfall producing relatively deeper snow accumulations. Snowmelt may occur during the winter period and early spring. Researchers have monitored the reduction of snow cover in Canada and trend of early snowmelt season and have predicted the continuing decrease through 2025 using climate models (Mudryk *et al.*, 2017). Moreover, the dominant factor controlling inter-annual variability of snow cover in Southern Ontario is changing to surface temperature rather than precipitation events (Mudryk *et al.*, 2017). With potential influences from climate change, abnormal winters occurred in Southern Ontario recently with extreme events such as warm temperatures and snowstorms, which might increase flood events, decrease the sustainability of ecosystem and infrastructures (Mortsch *et al.*, 2006). Therefore, monitoring snow cover for this region is important, and unusual snowmelt events can be an indicator of changes to come.

The study area covers majority of Southern Ontario as the coverage of available Sentinel-1A images from 2014-2017 (Figure 3.1).

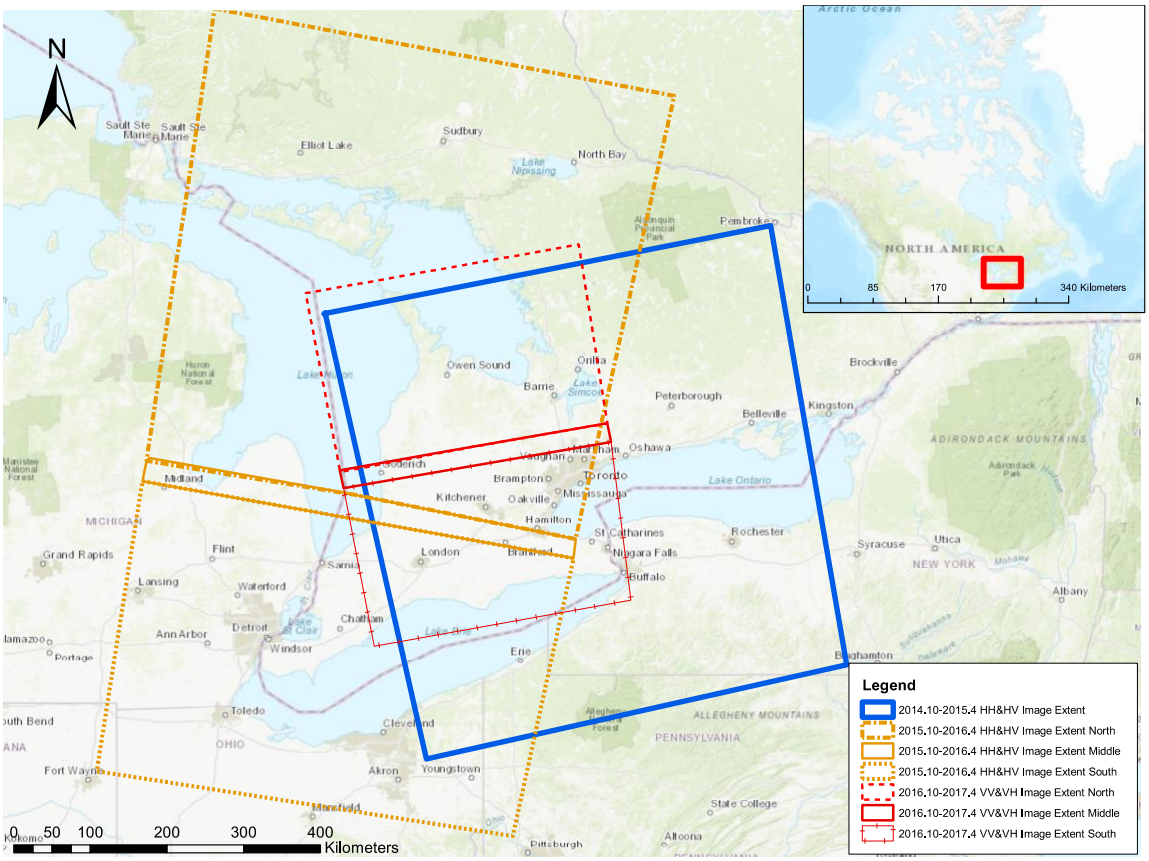

Figure 3.1 Study Area with Different Image Coverage for Different Time Periods

3.2 Data

3.2.1 Sentinel -1A Radar Images

43 Sentinel -1A C-band radar images were acquired for this study from 2014 to 2017. Due to the data availability, dual polarized images from different modes and polarizations were obtained. To eliminate the influences of trees and grasses in the summer, the Nagler and Rott method (2000) suggested to only use images from the same winter period as inputs for the wet snow detection. Therefore, the images used in this study for a winter period were all from the end of October to the end of April with revisit time of 12 days. There are 14 images of 2014-2015 and 14 images of 2015-2016 acquired from GRD EW mode with a swath width of around 400 km from HH&HV polarization. Additionally, 15 images of 2016-2017 acquired from GRD IW mode with a swath width of around 250km from VV&VH polarization. All the images are in the Level-1 Ground Range Detected (GRD) product format, which have been focused, multi-looked and projected into the World Geodetic System 1984 (WGS84). HH&HV images are medium resolution GRD

products with pixel spacing of 40m * 40m, and VV&VH images are high resolution GRD products with pixel spacing of 10m * 10m.

The incidence angles for EW mode is in a range of 18.9° - 47.0°, and IW mode is around 31° to 46.0°. Based on the different footprints of the images, one or two images from the same date were acquired to maintain the consistency of the study area coverage. The footprints of different image coverages are presented in Figure 3.1. The middle areas were generated from the shared areas of southern and northern images of different days. Appendix A lists the radar datasets used in this study

3.2.2 Meteorological data

The weather station datasets were acquired from historical climate datasets at Environment Canada (http://climate.weather.gc.ca/historical_data/search_historic_data_e.html). Data were automatically accessed and saved by a script and included hourly air temperature and daily snow depth on the ground for the days with Sentinel-1A observations. The temperature was acquired for the specific time when the Sentinel 1A image was captured based on the metadata and was in degrees Celsius (°C). Snow depth was daily snow depth on the ground measured in cm, and the snow depth less than 0.2 cm is called a "Trace". When the temperature data is missing on the specific time, an average of the previous and later hour temperature is used (if available).

Due to the availability of the datasets, there were temperature data from 35 weather stations, and snow depth measurement from 58 stations for Southern Ontario. However, to keep the consistency of time and location, only the stations that have continuous data from 2014 to 2017 within the coverages of three year' images were kept. In total, there were 18 stations selected, with the locations presented in Figure 3.2. Overall for 43 days with 18 stations, there were no missing values for temperature, but there were 157 records missing for snow depth data.

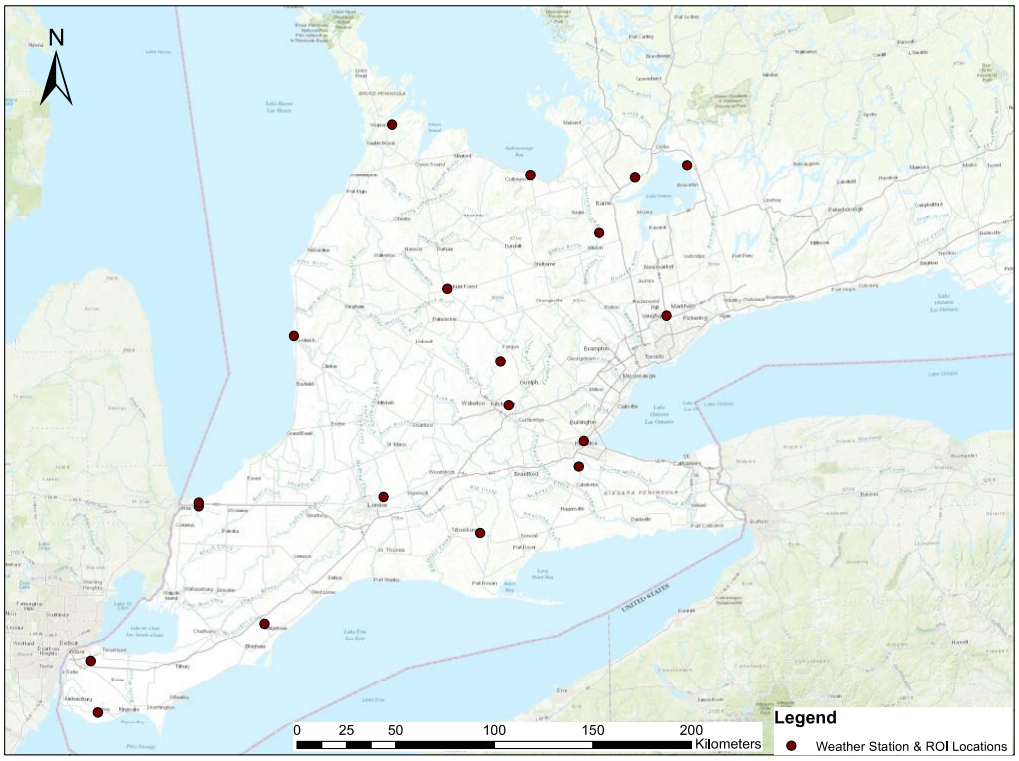

Figure 3.2 Weather Station Location Map

3.2.3 MODIS Snow Cover Product MOD10L2C

The MODIS/Terra Near Real Time (NRT) Coarse Snow Cover 5-Min L2 Swath 5km (MOD10L2C) provides the coverage of snow for each pixel in a resolution of 500m. MODIS snow cover product were generated from a snow mapping algorithm, which applied the Normalized Difference Snow Index (NDSI) and other physical criteria (NASA, 2017). The binary snow cover map indicated the existence of snow with pixel value of 1, whereas 0 stands for no snow.

3.3 Methodology

3.3.1 Preprocessing

Several preprocessing steps were applied on the Sentinel 1-A GRD images to reduce the speckle noises and standardize the images. Sentinel 1-A images were imported into the Sentinel Application Platform (SNAP) produced by ESA. An automatic workflow was conducted with the graph builder. The first step was to apply precise orbit files loaded from SNAP's server, which can update the orbit state vector for more accurate information. To standardize the backscatter values, the images were calibrated to sigma nought (σ^o). Then, to reduce the speckle noise, a Refined Lee Speckle Filter was applied which not only reduces speckle but also preserves edges and point target

signatures (Lee *et al.*, 2006). For VV & VH images, an extra step of multi-looking, which used four ranges and four azimuth looks, was employed to reduce the large processing size and to make the pixel size around the same as the HH & HV images for further comparison. For the images within the same footprint, co-registration was performed based on the ground-control points to align the images in a pixel basis, and the co-registered images were generated into one stack. A multi-temporal speckle filter was applied on the image stack to reduce speckles in a temporal manner.

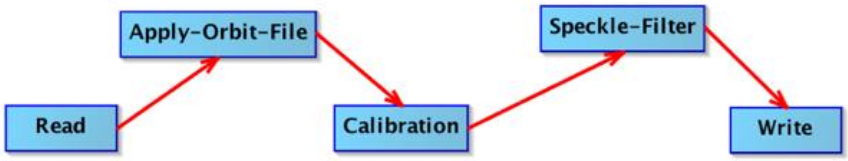

Figure 3.3 Graph Builder Workflow for HH&HV Images

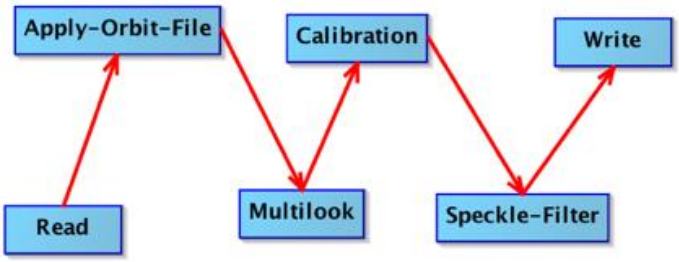

Figure 3.4 Graph Builder Workflow for VV&VH Images

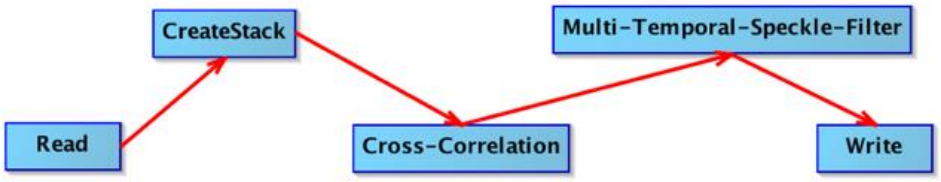

Figure 3.5 Workflow of Co-registration

3.3.2 Calculation of Reference Image

Based on the change detection method of Nagler and Rott (2016), the selection of reference image is critical for identifying the wet snow. As suggested by the previous studies, an average of images without wet snow in the winter period is suitable to serve as a reference (Nagler *et al.*, 2016). Due to the definition and physical properties of wet snow, when snow depth is greater than 0 cm and temperature is above 0 °C, potential existence of wet snow can be assumed. Therefore, using the weather station temperature data, potential wet snow days were identified and summarized in Table 3.1. The images from the three winter periods were in different coverages, therefore, a reference image was calculated for each coverage by averaging the images from the days without potential wet snow.

Table 3.1 Potential Wet Snow Days

Year	Dates
2014	11.22, 12.16, 12.28
2016	1.25, 3.25, 4.6, 12.22
2017	1.3, 1.15, 2.20, 4.9

3.3.3 Calculation of Ratio Image

Because of the decreased backscatter from wet snow compared with that from non-wet snow, the differences between an image with potential wet snow and the reference image are able to provide clues of existence of wet snow. Therefore, the ratio between an image with potential wet snow and the reference image of the same polarization can be calculated as:

$$Ratio(dB) = 10 * \log10(\frac{\sigma^o\ (intensity)}{\sigma^o_{reference}\ (intensity)}) \quad (3.1)$$

To examine the influences from the terrain, a Range Doppler Terrain Correction was applied on all the images, which compensates the distortions from the terrain. As there were no wet snow mapping studies for this study area, an experimental threshold of -2dB from Nagler (2016) was applied to generate a first estimate binary snow map, where a pixel with a ratio less than -2 dB was defined as wet snow:

$$Ratio(dB) < -2 \text{ dB} \quad (3.2)$$

3.3.4 Regions of Interest (ROIs) Analysis

ROIs were selected to further evaluate the change detection results by analyzing the backscatter patterns of different polarizations and time periods and influences from terrain. Because the study area has variations in land cover types and geophysical properties, to obtain more homogeneous characteristics of the ground, agricultural lands were chosen as the ROIs. Moreover, the ROIs were created adjacent to weather stations so that the weather datasets could be seen as the ground reference. Each ROI was a 3*3-pixel neighbourhood around the weather station producing a total of 18 ROIs, within the study area (for locations see Figure 3.2). To understand the relationships between ratio, polarization and incidence angle, the statistics were evaluated for each ROI. The summarized values were calculated by averaging the values of the pixels in each ROI. Table 3.2 lists the ROIs for each image by winter period. Along with the closest weather station to the ROI. North, south and middle refer to the different image extents shown in Figure 3.1.

Table 3.2 ROI Distribution

2015-2016 HH&HV	**2014-2015 HH&HV**	**2016-2017 VV&VH**	**Adjacent Weather Station**
North ROI 1	ROI 4	South ROI 4	Hamilton RBG CS
North ROI 2	ROI 5	South ROI 5	Kitchener Waterloo
North ROI 3	ROI 6	South ROI 6	Elora RCS
North ROI 4	ROI 7	Middle ROI 1	Goderich
North ROI 5	ROI 8	North ROI 1	Mount Forest (AUT)
North ROI 6	ROI 9	North ROI 2	Wiarton A2
North ROI 7	ROI 10	North ROI 3	Collingwood
North ROI 8	ROI 11	North ROI 4	Egbert CS
North ROI 9	ROI 12	North ROI 5	Barrie
North ROI 10	ROI 13	North ROI 6	Lagoon City
	ROI 14	South ROI 7	Toronto Buttonville A
South ROI 1	ROI 2	South ROI 2	Delhi CS
South ROI 2	ROI 1	South ROI 1	London CS
South ROI 3			Ridgetown RCS
South ROI 4			Harrow CDA
South ROI 5			Windsor A
South ROI 6			Sarnia
Middle ROI 1	ROI 3	South ROI 3	Hamilton A

3.3.5 Sensitivity Analysis

To analyze the performance of different thresholds, a sensitivity analysis was conducted. A series of thresholds of -0.5, -1, -1.5 and -2.5dB was tested on the ratio images. To analyze the influences from temperature near freezing point and shallow snow on determining the wet snow, temperature and snow depth for wet snow were plotted for each threshold. Because the reciprocity assumption applies in the case of monostatic SAR systems, cross-polarizations can be seen as the same. Therefore, ratios from cross-polarizations (HV and VH) were assumed equal.

3.3.6 Evaluation

In order to evaluate the effectiveness of the thresholds, accuracy assessment was performed for each year and each polarization. As the ROIs were created adjacent to the weather stations, the temperature and snow depth information were used as the reference "truth". While some of the snow depth datasets were missing, MODIS snow products were added to confirm the existence of snow. Confusion matrices (Congalton, 1991) were generated based on the number of according matched ROIs. To evaluate the performance of the threshold, accuracy, precision, recall and the F1 score were calculated for each polarization of each winter period. To demonstrate the calculation of these metrics, an example confusion matrix is showed in Table 3.3.

Table 3. 3 An Example Confusion Matrix

	Predicted Positive	Predicted Negative
Actual Positive	True Positives (TP)	False Negatives (FN)
Actual Negative	False Positives (FP)	True Negatives (TN)

Accuracy refers to the overall correctness of both wet and non-wet snow identification, which is the ratio between the correctly predicted wet and non-wet snow and the total pixels, it lies in a range of 0 to 1. An accuracy of 1 means all the wet and non-wet snow are correctly predicted, and an accuracy of 0 means there are nothing predicted and can be calculated as:

$$Accuracy = \frac{TP+TN}{TP+FP+TN+FN} \tag{3.1}$$

Precision is the ratio between correctly predicted wet snow and the total predicted wet snow and non-wet snow for the sample and ranges between 0 and 1. A precision of 0 means that there are no

existing wet snow pixels correctly classified. A precision of 1 means that all existing wet snow pixels are correctly classified and that there are no false positives. Precision is calculated thus:

$$Precision = \frac{TP}{TP+FP} \tag{3.2}$$

Recall is the ratio of the number of correctly predicted wet snow sample pixels to the total number of true wet snow population pixels and falls into a range of 0 to 1. A recall of 0 means there is nothing classified as wet snow even though there are wet snow pixels present, and a recall of 1 indicates that all the wet snow pixels are correctly classified. Recall can be calculated by:

$$Recall = \frac{TP}{TP+TN} \tag{3.3}$$

The F1 score is a weighted average of precision and recall, where the contribution from precision and recall are equal, and is calculated as:

$$F1 = 2 * \frac{Precison*Recall}{Precison+Recall} \tag{3.4}$$

3.3.7 Classification

Studies have successfully shown that classification approaches can yield robust wet snow mapping results (Huang *et al.*, 2011). Therefore, the ratio threshold method was compared with a classification approach applied to the ratio images. Because the 2014-2016 winter images were greatly influenced by incidence angles, the classification was only applied on 2016-2017 winter images. Therefore, there were 10 ratio images involved in total. Labels of images were generated by identifying agricultural land with wet snow or not wet snow near the weather stations. A 9*9-pixel area was searched for agricultural land surrounding each weather station pixel. Most meteorological variables such as temperature and humidity can be similar in a local scale of around 50km, while sometimes there might be transitions in a short distance within 10km (Van der Voet, 1994). Therefore, to obtain homogeneous weather conditions, it was assumed that the 360m*360m area can relatively accurately represent the measured meteorological conditions from a weather station in our study area. For the convenience of processing and the limited influences from terrain of the ROI areas, the features used in the classification were ratio images from co- and cross-polarizations without terrain correction. In the weather records of 14 stations for 5 days, there were 41 out of 70 records with wet snow, so that datasets generally had balanced amount of wet and

non-wet snow. Two supervised classifiers were used to compare with each other. First, logistic regression (LR) was used. This is a binary classifier which estimates the likelihood of a pixel class membership based on a maximum likelihood (Menard, 2018). Support Vector Machine (SVM) is a non-parametric approach based on the statistical learning theory by finding a hyperplane that is at a maximum distance from the nearest points from the two classes to better separate the datasets (Vapnik, 1995). SVM was chosen because of its capability of identifying non-linear boundaries using small number of sample datasets (He *et al.*, 2015). A Radial Basis Function (RBF) kernel SVM was used in this study. To validate the performance of the classifiers, cross-evaluation was employed to separate the obtained datasets for training and testing purposes. A ten-fold cross-evaluation was used to split the labeled pixels into 10 consecutive folds, where only one of the subgroups was used for testing while the others were used for training each time. The accuracy assessment was given by averaging the modelling metrics of each fold. Accuracy, precision, recall and f1 score were included in the metrics. A parameter C, a penalty parameter that "trades off misclassification of training examples against simplicity of the decision surface" ("RBF SVM Parameters", 2017), was tuned for each classification to find the best accuracy, which was then compared with the threshold results. Although the classifications were applied to the whole scene, there were varying coverages of snow in the whole scenes, with many more non-wet snow pixels than wet snow pixels. As the model was built based on balanced datasets, the application on the whole scene would likely bring more misclassifications of non-wet snow into wet snow.

The models output the probability of a sample (a pixel) belonging to wet snow. The probability ranges from 0 to 1, where a threshold can be used to determine whether the pixel was classified as wet snow or non-wet snow. The simple default thresholds for logistics regression and SVM is 0.5. As part of the threshold tuning process, a recall and a false positive ratio can be obtained for each threshold. The false positive rate is calculated as:

$$FP = \frac{FP}{TN+FP} \tag{3.5}$$

A receiver operating characteristic (ROC) curve can be generated by having false positive rate as x-axis and recall as y-axis, which shows the trade-off between these two metrics (Fawcett, 2006). Plotting the ROC curve is a common method to deal with the imbalanced datasets and to help tune the probability of threshold (Sun *et al.*, 2009). Since the datasets from whole scenes were heavily imbalanced, a high false positive ratio will likely result in a large number of misclassifications of

non-wet snow. By trading off some portion of the recall, the false positive ratio should be reduced. Therefore, ROC curves for classifiers were generated to understand the relationship between recall and false positive rate. Moreover, precision and recall curves were also plotted to observe the influences of trade-off on recall. Due to the imbalanced data for the whole scene, the default threshold of 0.5 needed to be adjusted. Having determined the threshold, binary snow maps were generated by applying the classifiers onto the whole study area. The classification process was implemented in Python with Scikit-learn library.

The workflow for methodology is shown in Figure 3.6. Figure 3.6 (a) presents the workflow for the change detection, and (b) shows the factors analyzed in ROI analysis and (c) shows the classification workflow.

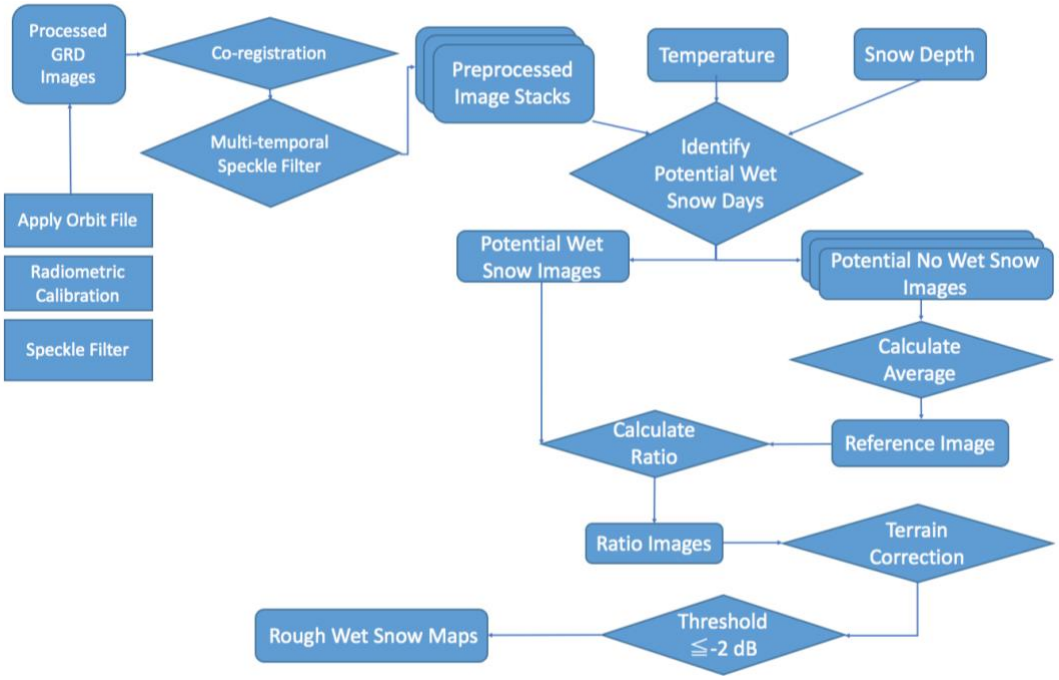

(a) Change Detection Workflow

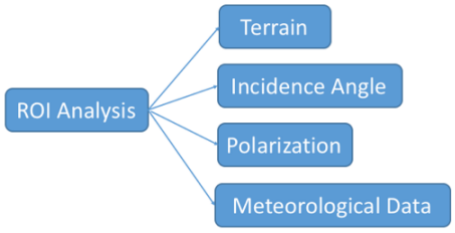

(b) Factors Analyzed in ROI Analysis

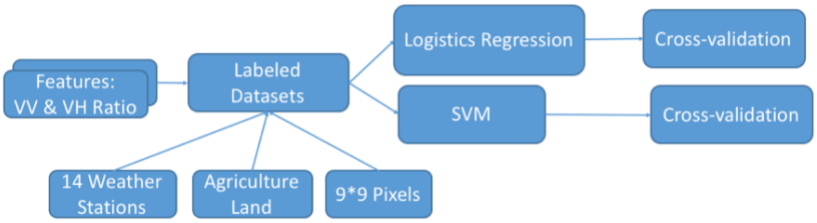

(c) Classification Workflow

Figure 3.6 Methodology Workflow

Chapter 4 Results

4.1 Standard Thresholding Results

Binary wet snow maps were generated for each polarization by applying the -2dB threshold on the ratio images. Figure 4.1 shows an example of the ratio images and binary wet snow maps for December 16, 2014. From the ratio images, the distribution of low backscatters could be observed from the explicit dark areas in the middle from both polarizations, whereas the southern areas were bright. From the binary snow maps, potential wet snow distributed near Barrie and Lake Simcoe, while there were little in southern areas. Figure 4.2 shows all binary snow maps from 2014 to 2017, and a modeled snowpack temperature map from NOAA SNODAS products each day for the nearest time to the time when the S1A image was captured was also presented to demonstrate the distribution of snow. Generally, the distribution of identified wet snow roughly aligned with the existence of wet snow. It can be observed that on November 22, 2014, the binary map for HV shows larger areas of existence of wet snow than HH images, which aligns with the existence of snow cover. December 28 identifies wet snow in the middle areas where snow cover map shows none. Binary maps of January 3, 2017 show more wet snow in southern areas than in the north.

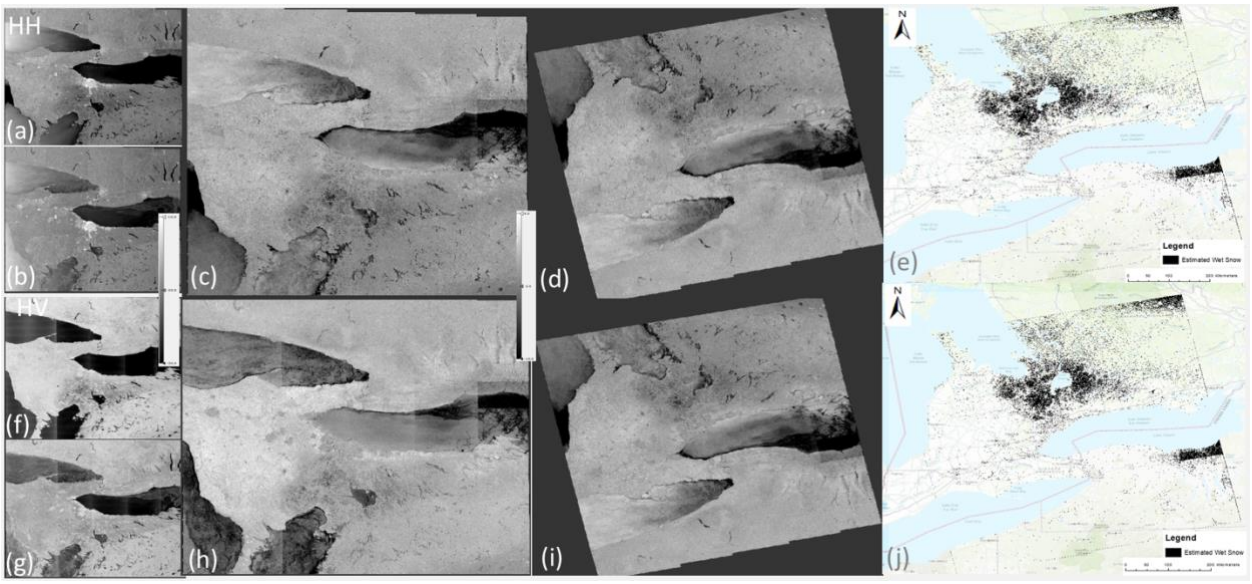

Figure 4.1 An example of change detection result from 23:07 UTC, December 16, 2014 (a) is the preprocessed σ^o HH polarized image; (b) is the reference image averaged from images without potential wet snow; (c) is the ratio image calculated from (a) and (b); (d) is the terrain corrected ratio image; (e) is the binary wet snow map from thresholding with wet snow represented in black against a basemap of land, water and forest cover ; (f)-(j) are the results for HV images.

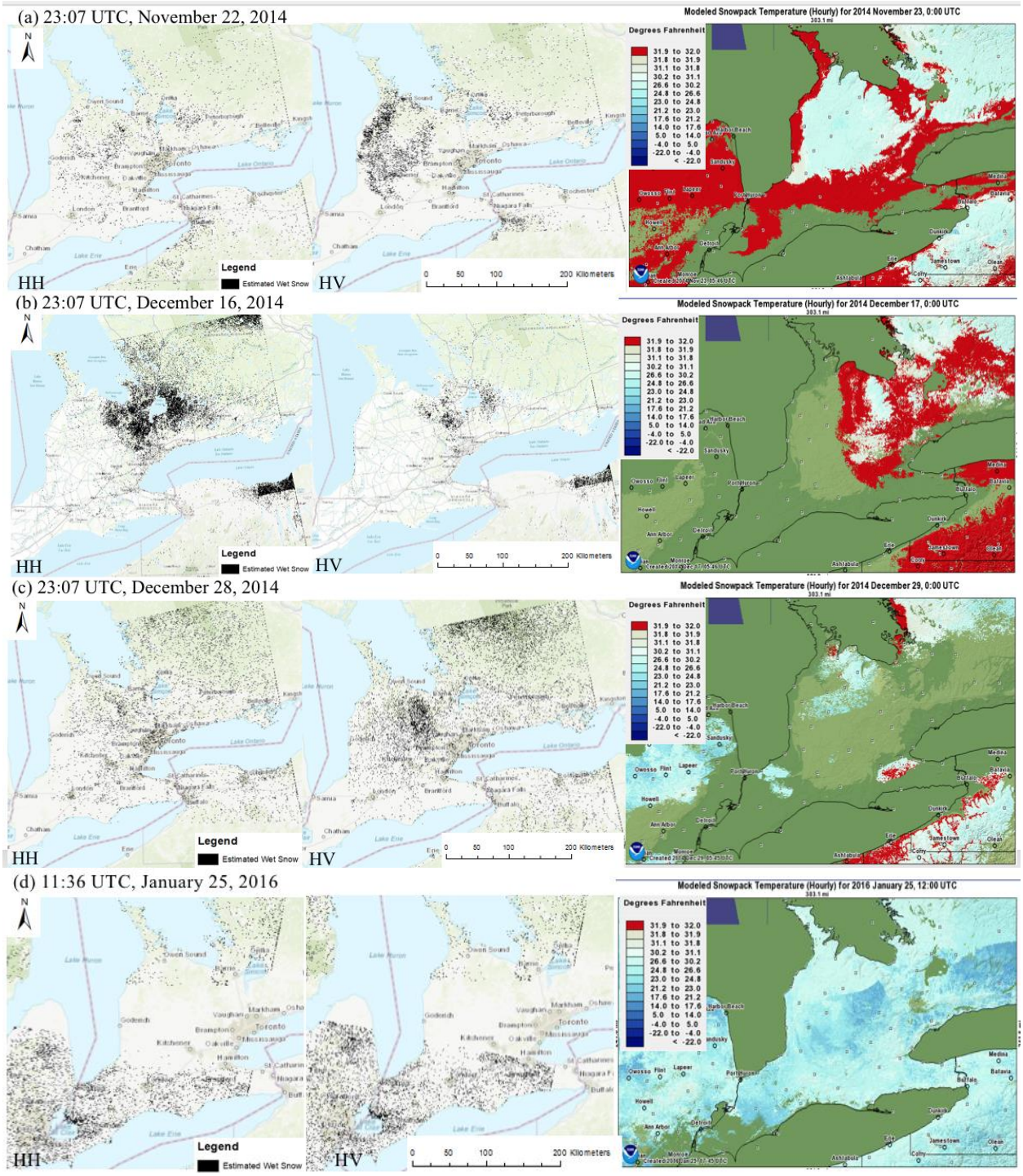

Figure 4.2 Binary snow maps of wet snow and NOAA SNODAS Snowpack Temperature maps. Each date (a) - (i), shows: wet snow from the co-polarization data (left); cross-polarized data (middle) with wet snow represented by the black pixels against a basemap of land, water and forest cover; SNODAS maps of snowpack temperature (right).

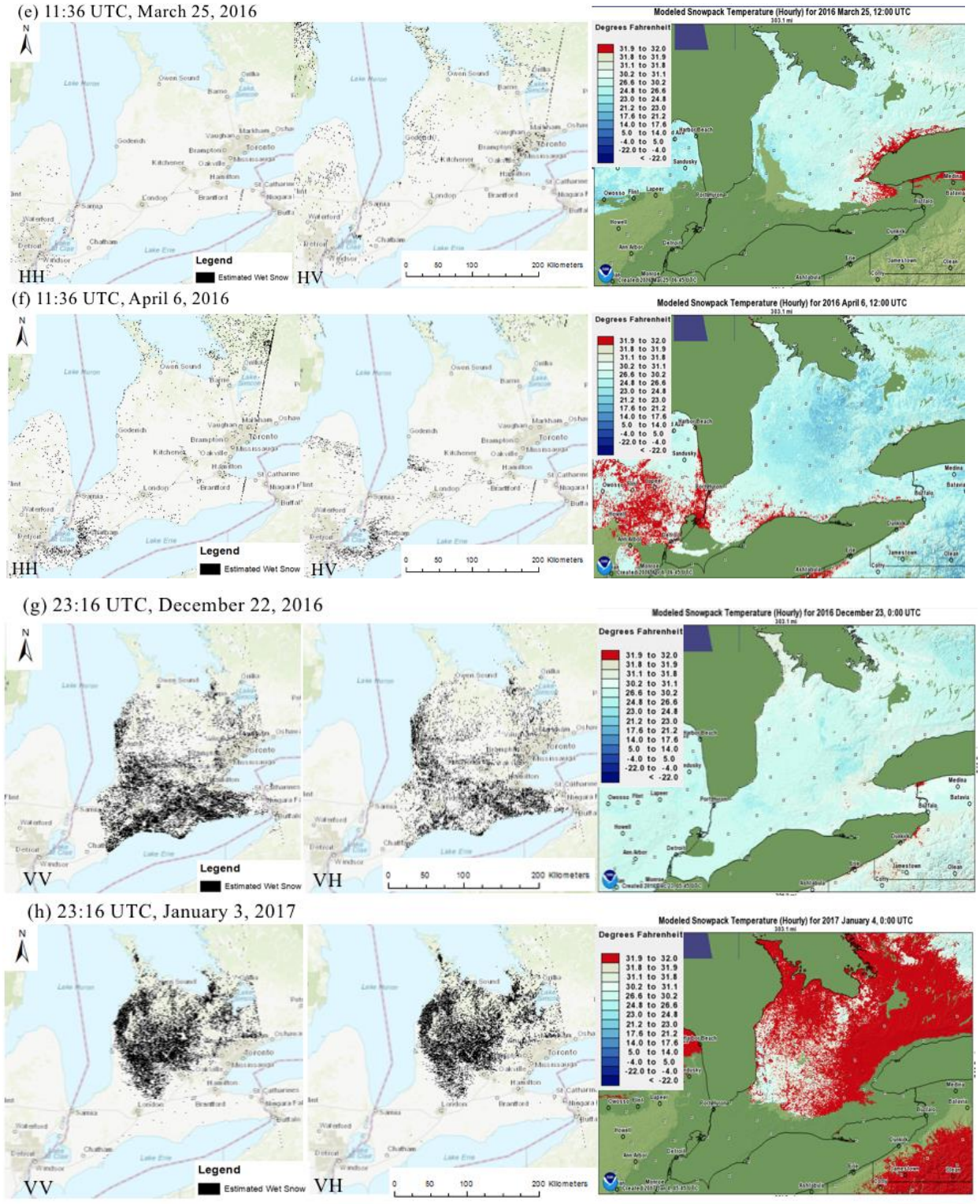

Figure 4.2 (cont.)

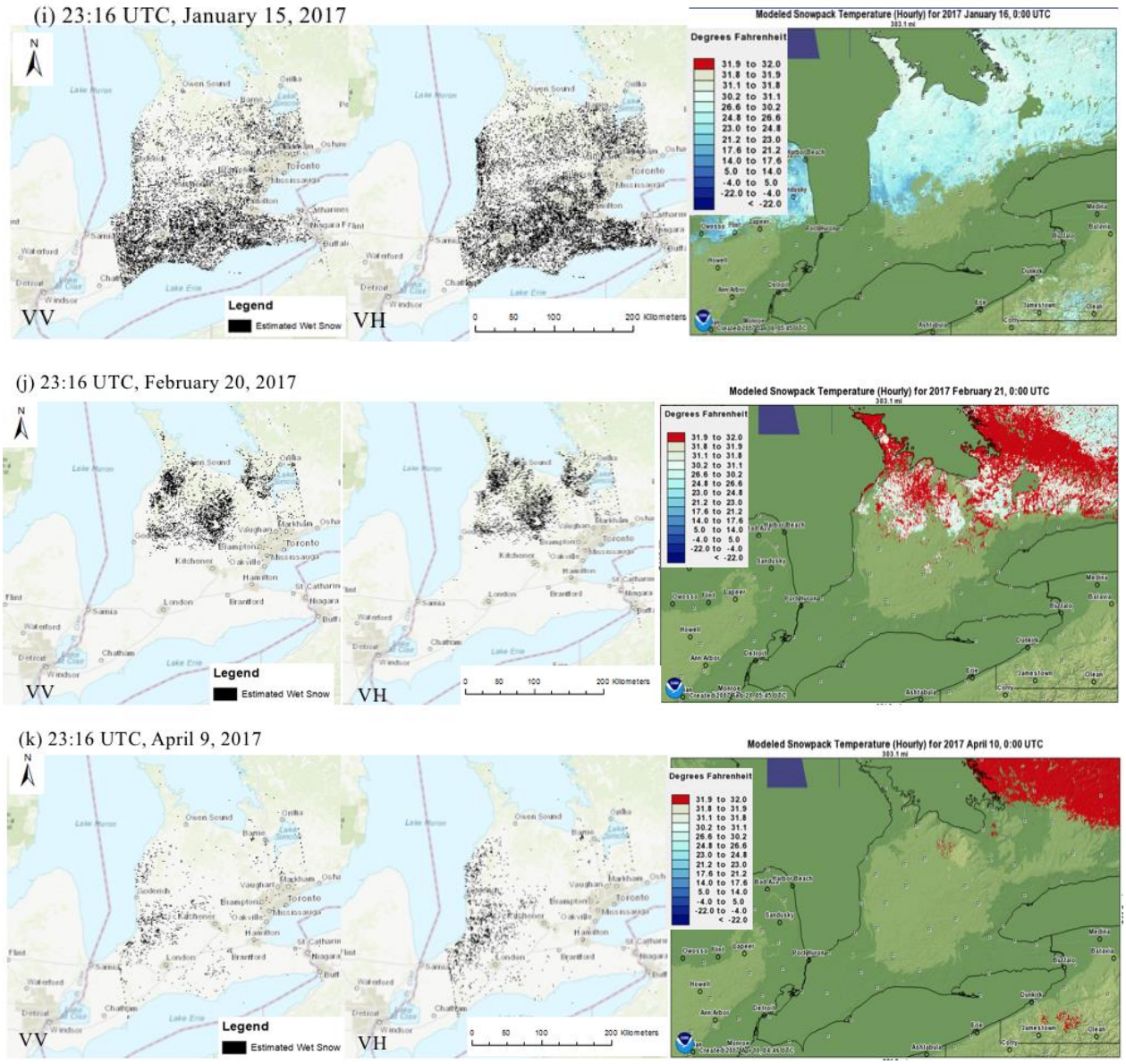

Figure 4.2 (cont.)

4.2 ROI Analysis to Determine Optimum Threshold

4.2.1 Ratio

The ratio values and wet snow conditions for each ROI is summarized in Appendix B. The table listed the average ratio values for the ROIs from dates with potential wet snow (listed in Table 3.1) and identified if there was wet snow or not based on ground reference datasets.

4.2.2 Influences from Terrain

The pixel ratio values from equation 3.1 of ROI pixels were recorded before and after terrain correction to compare the influences from terrain of the study area on the ratio values. Since the terrain of the ROIs were relatively flat and gently undulating, the terrain should not influence the ratio values. By summarizing the statistics, it can be observed that the ratios did not change significantly, which indicated that the terrain correction did not influence the ratio values. Figure 4.3 shows the comparison of ratios before and after terrain correction for each year. The graphs show that the relationships between the uncorrected and corrected image ratio data are very strong and fall along the 1:1 line of agreement. This was for both co- and cross-polarized image data. The average backscatter values are calculated and summarized in Table 4.1, and the values are relatively similar. Standard error is also calculated for each pair of comparison and summarized in Table 4.1, and the values are relatively small, which indicate the less spread of data points and reliability of the mean (McCloskey & Ziliak, 1996). Therefore, these results indicated the small influence of terrain on backscatter values for this region. Additionally, terrain correction did not make huge changes for both cross and co-polarization.

Figure 4.3 Comparisons of Ratio before and after Terrain Correction for 2014-2017

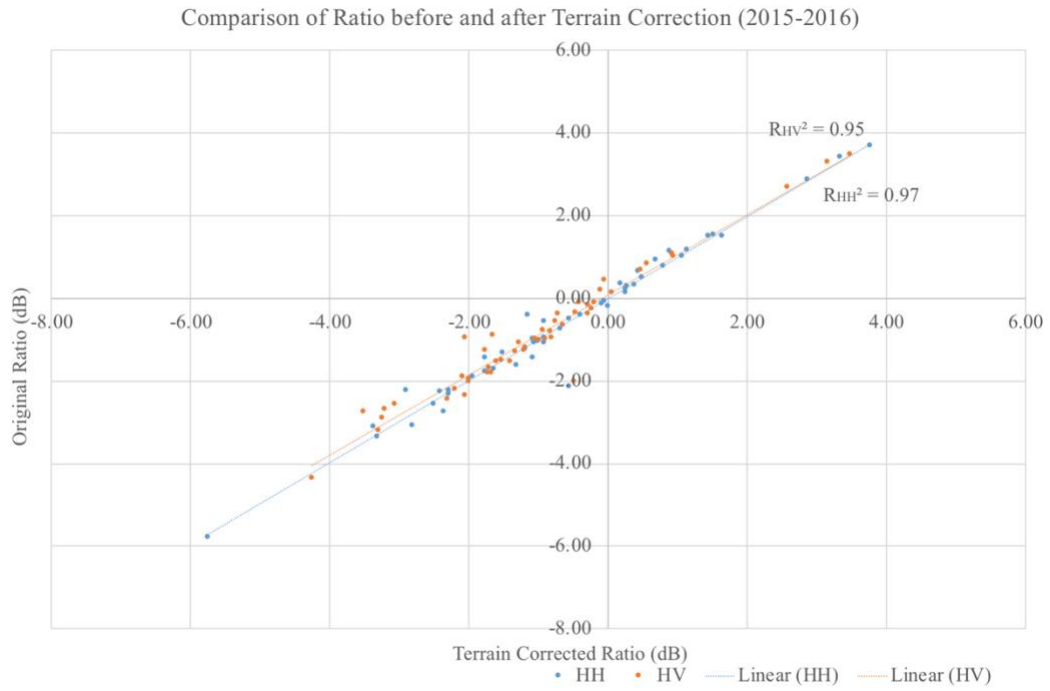

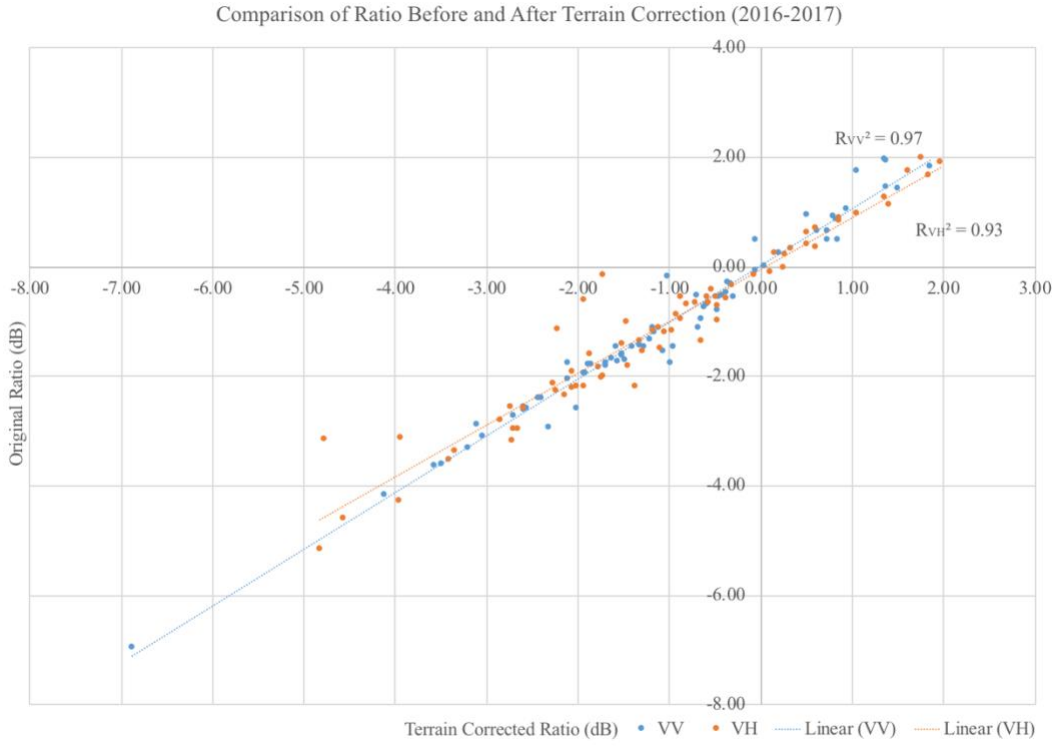

Figure 4.3 (cont.)

Table 4.1 Average Backscatter before and after Terrain Correction

Year	Polarization	Original	Terrain Corrected	Standard Error
2014-2015	HH	-0.83 dB	-0.80 dB	0.30
	HV	-0.26 dB	-0.24 dB	0.46
2015-2016	HH	-0.60 dB	-0.62 dB	0.31
	HV	-1.02 dB	-0.89 dB	0.36
2016-2017	VV	-1.10 dB	-1.08 dB	0.26
	VH	-1.11 dB	-1.12 dB	0.43

4.2.3 Relationship between Local Incidence Angle and Ratio

To understand the influences from local incidence angles, the relationships between ratio of wet snow and local incidence angle is plotted in Figure 4.4. The first two plots summarize ratios from HH and HV polarized images for 2014 to 2016. Trend lines are generated based on the median values for each incidence angle range. There are some tendencies that can be observed. The slope of the trend line for HH polarization is steep, where the ratios tend to decrease with the increased incidence angle, although it flattens out after around 30°. Rations from HV generally remain negative with little influences from the angle as shown by the gentle sloping trend line. The last two plots are generated from VV and VH polarized images for 2016 to 2017, and the slopes of the trend lines are relatively flat, which do not show great variations from positive to negative values with the incidence angles.

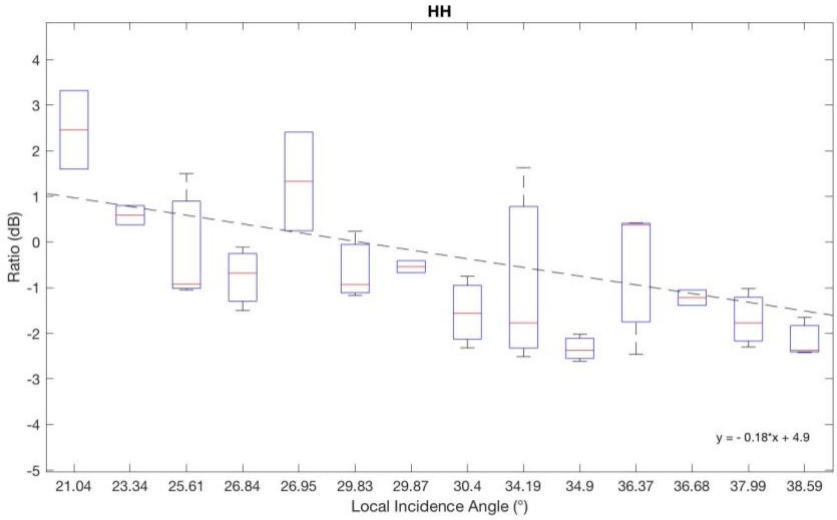

(a)

Figure 4.4 Local Incidence Angle and Ratio of Wet Snow for (a) HH Polarized Images, (b) HV Polarized Images, (c) VV Polarized Images and (d) VH Polarized Images

(b)

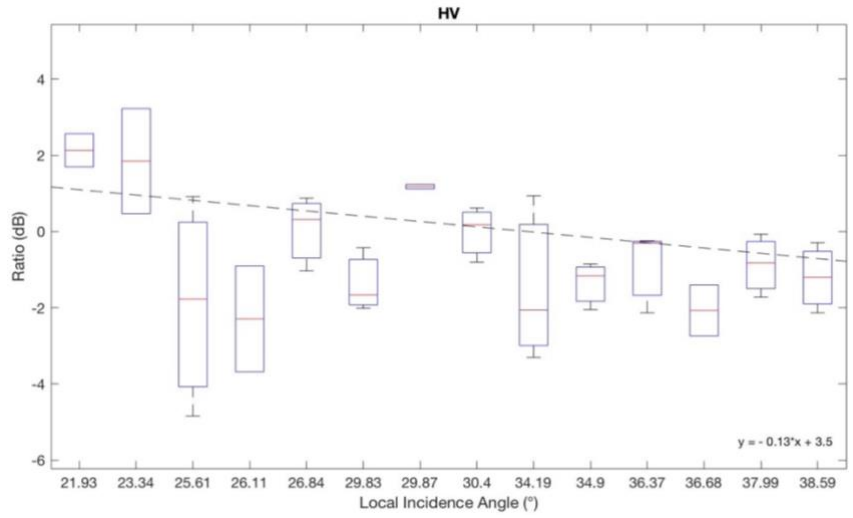

(c)

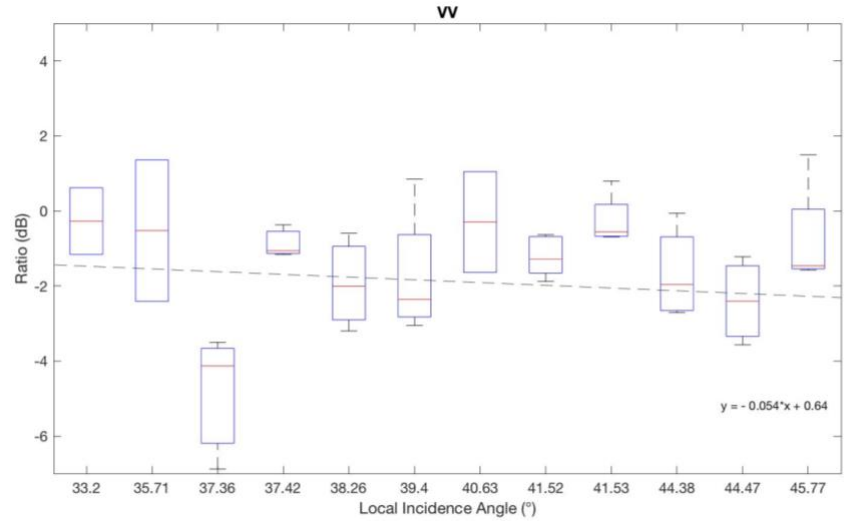

(d)

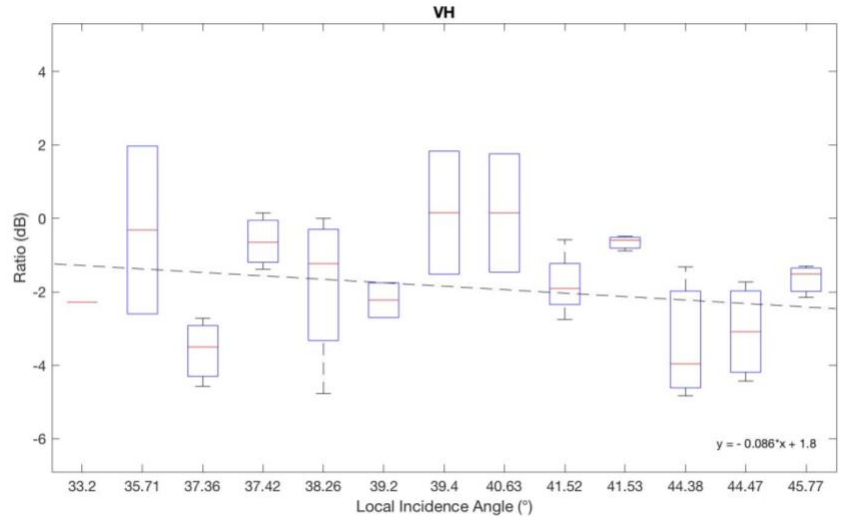

Figure 4.4 (cont.)

4.2.4 Variations of Temperature and Snow Depth

Because the incidence angles had great influences on images from 2014-2016, only the ratios from the ROIs with incidence angles over 30° were used in exploring temperature and snow depth relationships. Additionally, only the ROIs contained potential wet snow with available snow depth and temperature were examined. The trace snow depth was represented as 0.1cm. Moreover, the weather datasets for the thresholds from the sensitivity analysis were also plotted. The temperature and snow depth are plotted for VV and VH/HV in Figure 4.5. All the points plotted were identified as wet snow from the meteorological data, where the blue dots represent the classified wet snow from threshold, and red dots represent non-wet snow. It can be observed that the number of misclassified wet snow decreases with the increase of threshold, and the misclassified wet snow are mainly distributed in the boundary of freezing point of temperature and shallow snow depth. The plots indicate the influences of shallow snow depth and near freezing temperature, which would result in higher ratio values of wet snow.

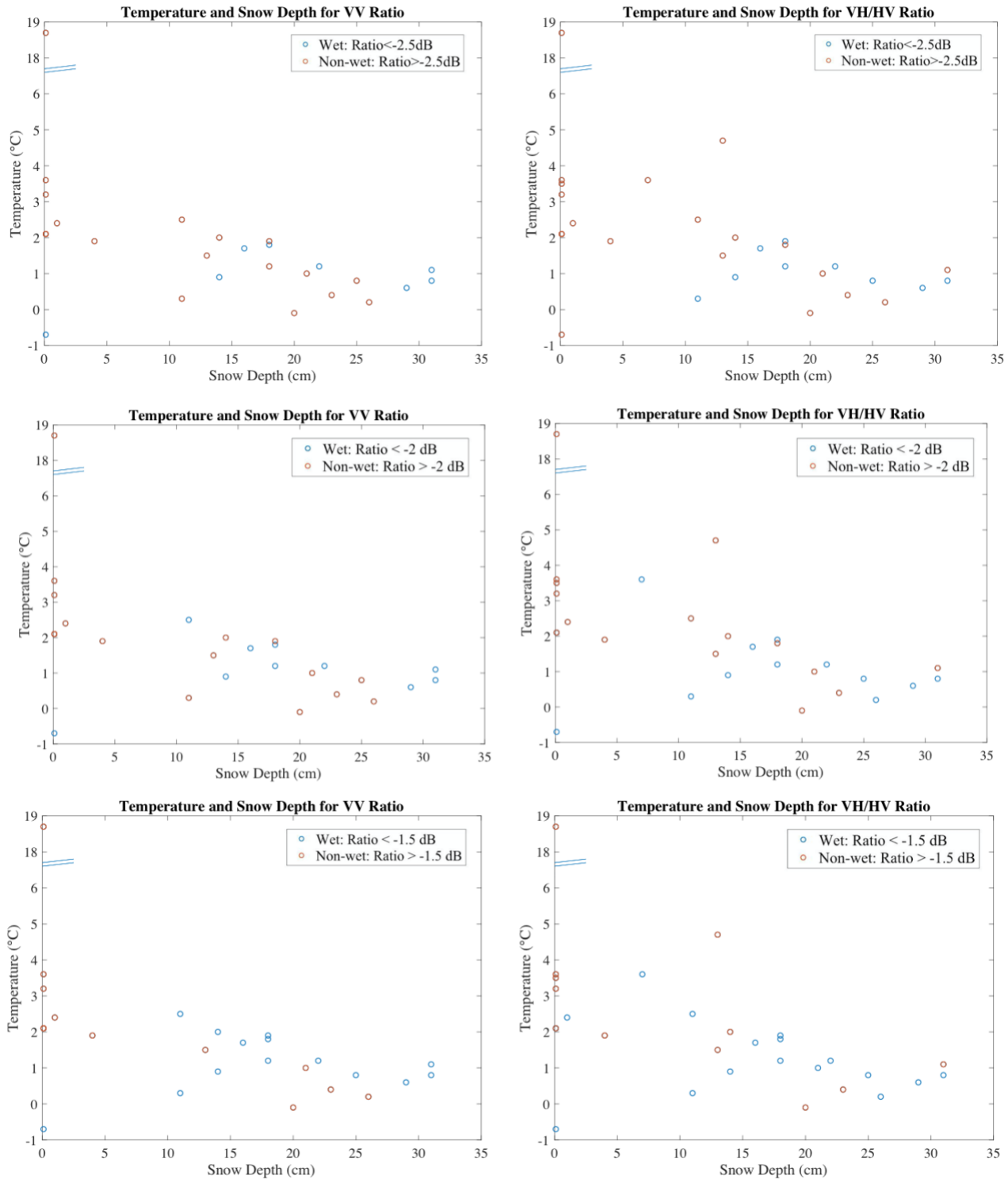

Figure 4.5 Temperature and snow depth for ratios from VV and VH/HV images. Each pair show the effect of a changing threshold from -2.5 dB to -0.5 dB. (see text for further explanation)

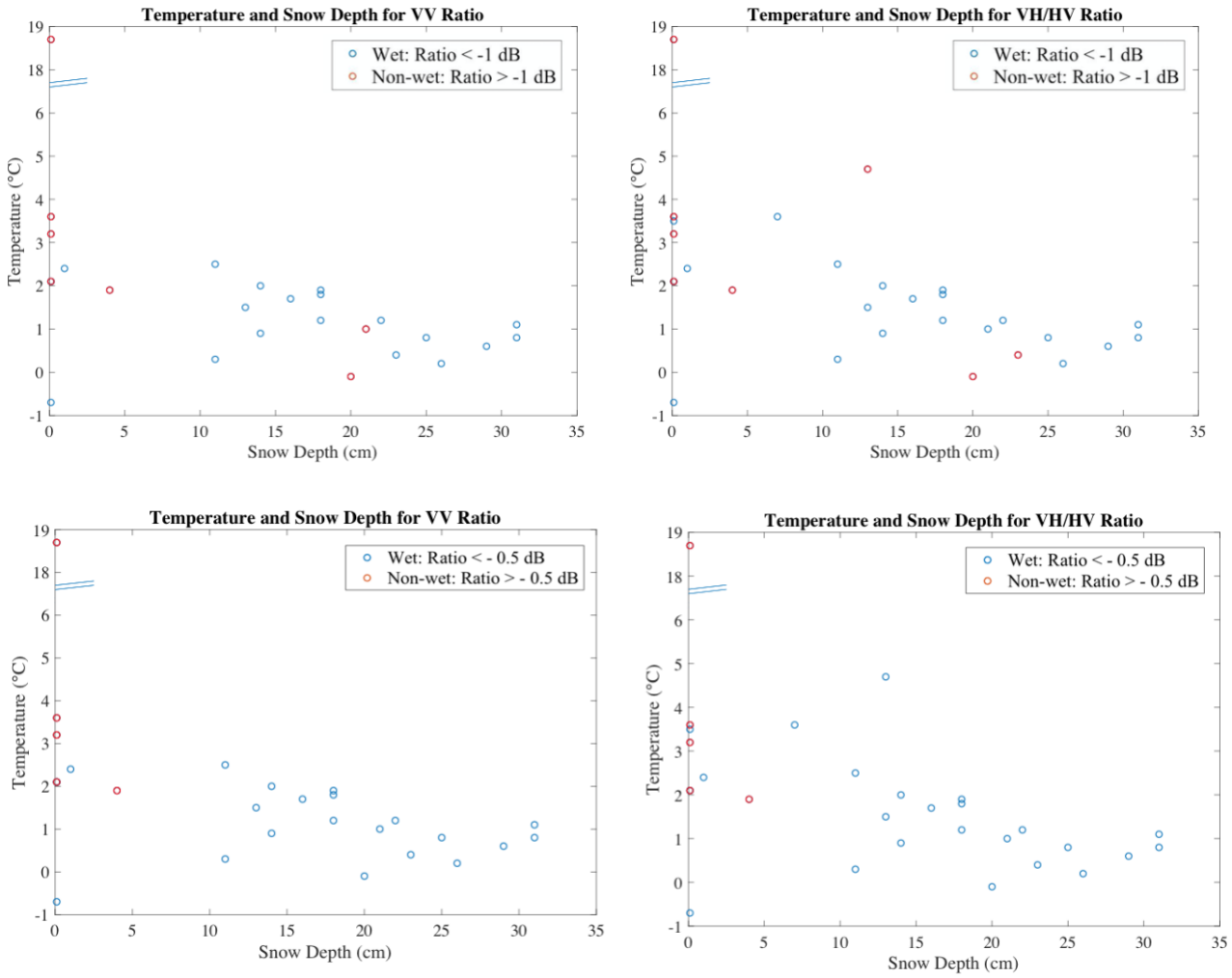

Figure 4.5 (cont.)

4.3 Evaluation of Thresholds for ROIs

The results from thresholding were compared with MODIS and weather data to assess the accuracy of thresholds. The accuracy assessment was done separately for each polarization and for each winter period. Thresholds of -2.5, -2, -1.5, -1 and -0.5 dB were tested individually to analyze the sensitivity of the datasets to different thresholds. Table 4.2 summarizes the precision, recall, F1 score and accuracies. The confusion matrices for each winter period can be found in Appendix C.

Generally, it can be observed that recall increases with increased threshold, which indicates the growing capability of identifying wet snow. However, it is at the expense of the misclassification

of non-wet snow into wet snow as the precision tends to decrease. It can be noticed that even though the first two years have higher accuracies than 2016-2017 for -2dB threshold, the precisions are relatively low, which indicates the low success of identifying wet snow. For HH/HV images, the overall accuracies reach highest at -2dB with relatively high precision and recall, while for VV/VH images, the accuracies are higher in -1 and -0.5 dB with higher precision and recall among other thresholds. It can also be found that cross-polarized images generally have higher accuracies than co-polarized images.

Table 4.2 Accuracy Assessment for Different Thresholds

(a) -2.5 dB Threshold

Image Year	Polarization	Precision	Recall	F1 Score	Accuracy
2014-2015	HH	0.2	0.05	0.08	0.48
	HV	0.5	0.11	0.18	0.55
2015-2016	HH	0	0	None	0.73
	HV	0.5	0.2	0.29	0.86
2016-2017	VV	0.89	0.2	0.33	0.53
	VH	0.85	0.28	0.42	0.56

(b) -2 dB Threshold

Image Year	Polarization	Precision	Recall	F1 Score	Accuracy
2014-2015	HH	0.6	0.32	0.42	0.6
	HV	0.5	0.16	0.24	0.55
2015-2016	HH	0	0	None	0.73
	HV	0.43	0.6	0.50	0.88
2016-2017	VV	0.75	0.3	0.43	0.54
	VH	0.8	0.4	0.53	0.6

(c) -1.5 dB Threshold

Image Year	Polarization	Precision	Recall	F1 Score	Accuracy
2014-2015	HH	0.57	0.42	0.48	0.6
	HV	0.5	0.16	0.24	0.55
2015-2016	HH	0	0	None	0.73
	HV	0.65	0.22	0.33	0.80
2016-2017	VV	0.67	0.45	0.54	0.56
	VH	0.75	0.53	0.62	0.63

(d) -1 dB Threshold

Image Year	Polarization	Precision	Recall	F1 Score	Accuracy
2014-2015	HH	0.43	0.47	0.45	0.48
	HV	0.43	0.32	0.37	0.5
2015-2016	HH	0.04	0.2	0.07	0.49
	HV	0.15	0.8	0.25	0.53
2016-2017	VV	0.68	0.65	0.66	0.63
	VH	0.70	0.65	0.67	0.64

(e) -0.5 dB Threshold

Image Year	Polarization	Precision	Recall	F1 Score	Accuracy
2014-2015	HH	0.43	0.47	0.45	0.48
	HV	0.43	0.32	0.37	0.5
2015-2016	HH	0.13	0.8	0.22	0.47
	HV	0.12	0.8	0.21	0.39
2016-2017	VV	0.66	0.73	0.69	0.61
	VH	0.67	0.78	0.72	0.66

4.4 Analysis of ROI Classification Results

It was found that different parameter C did not influence the performance of the models because precision, recall and accuracy were similar under different C. However, to obtain more generalized models, a default C of 1 was used for SVM and 0.023 was used for Logistic regression. From Figure 4.6 (a), it can be observed that when the recall is in the range of near 0.5 to 0.8, precision stays in a relative stable value of around the 0.7. When the false positive rate drops dramatically from 0.7 to 0.4, the recall (true positive rate) only decreases from 0.8 to 0.6. To obtain the low false positive rate, it is necessary to sacrifice some of the recall. A similar situation can be observed in Figure 4.6 (b) for SVM. Recall drops in a smaller range than that of logistic regression when the false positive rate decreases from 0.8 to 0.2.

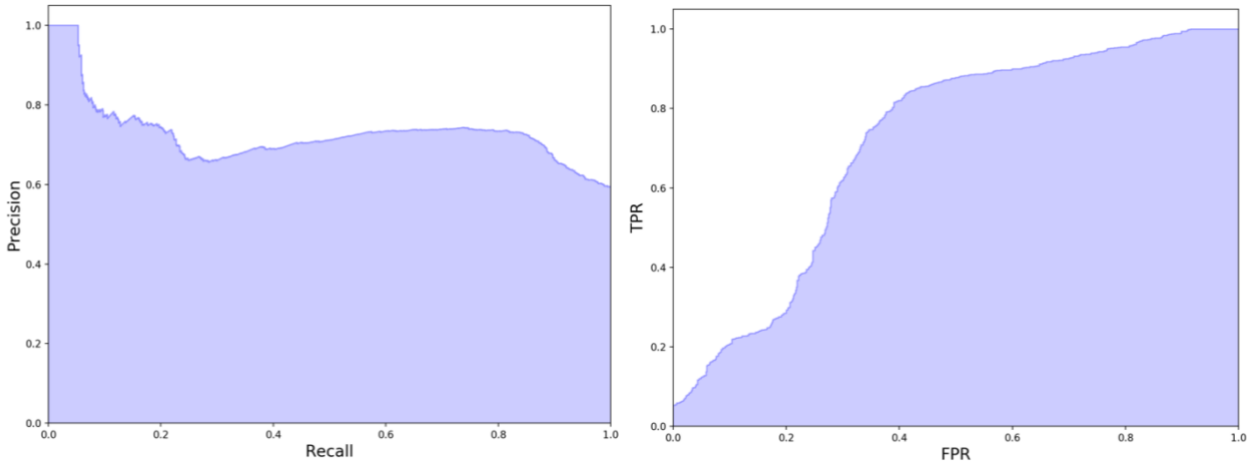

(a) Logistic Regression

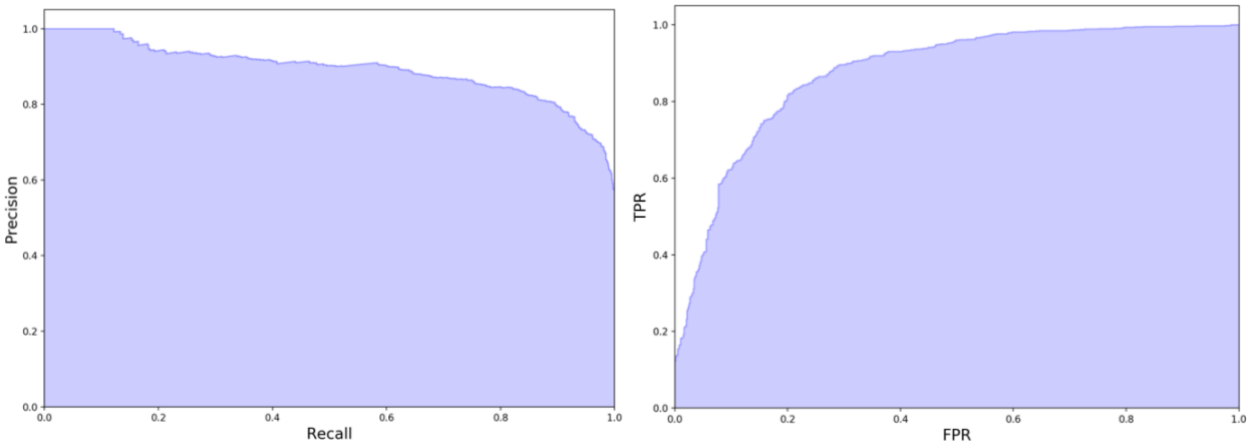

(b) SVM

Figure 4.6 Plots of Precision and Recall (left) and ROC Curves (right) for logistic regression (a) and SVM (b) classifications of ROIs.

To adjust the threshold of probability, a threshold of 0.6 was tested first. The accuracy assessment metrics for the cross-evaluations at different thresholds of probability for logistic regression and SVM are compared in Table 4.3. For logistic regression, it can be observed that false positive rate decreases with threshold of 0.6, while a relative high precision is remained. In the meantime, the recall also drops. Higher thresholds will result in lower recalls and precisions, so for logistic regression, the threshold of probability was adjusted to 0.6. While for SVM, from threshold of 0.5 to 0.6, the false positive rate does not decrease much. Thus, a threshold of 0.7 was tested as well, and it showed reduced false positive rate. Precision remained similar to that of threshold of 0.6, and recall was still kept still kept in a relatively high value. Therefore, to achieve the better classification result on the whole scene, 0.7 was a suitable threshold of probability for SVM.

Table 4.3 Classification Accuracies

	Logistic Regression		**SVM**			**Threshold (-2dB)**	**Threshold (-2dB)**
Threshold of Probability	**0.5**	**0.6**	**0.5**	**0.6**	**0.7**	**VV**	**VH**
Precision	0.73	0.72	0.82	0.84	0.85	0.7	0.81
Recall	0.84	0.56	0.86	0.83	0.77	0.26	0.3
F1 Score	0.78	0.63	0.84	0.84	0.81	0.38	0.42
Accuracy	0.73	0.63	0.81	0.81	0.79	0.53	0.61
False Positive Rate	0.41	0.27	0.22	0.21	0.17		

To further test the sensitivity of the ratio thresholding method, Figure 4.7 shows the changes of accuracies of thresholds from -5 to 5 dB with an interval of 0.01dB on the labeled datasets. It can be observed that with the increase of threshold, recall increases with the decrease of precision. Accuracy reaches the highest at threshold around 0.5dB.

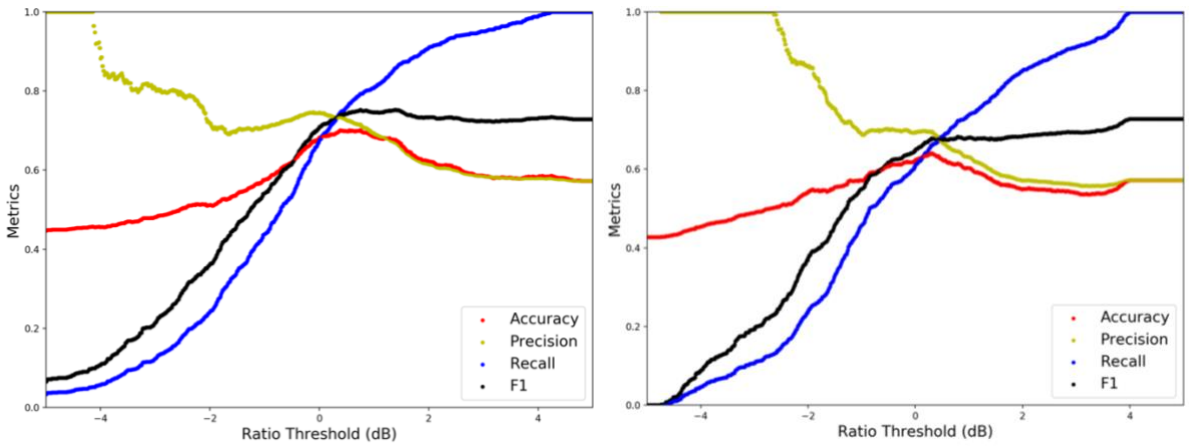

(a) VV (b) VH

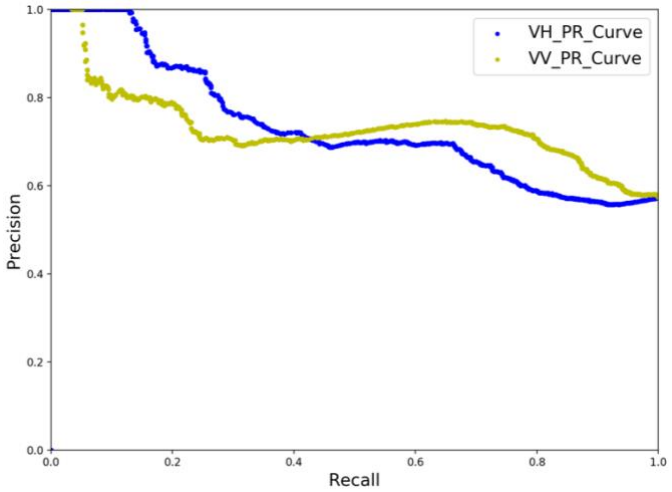

(c) Relationship between Recall and Precision

Figure 4.7 Changes of Accuracies with Ratio Thresholds

The distribution of ratio values and the identified classes from different classification methods are presented in Figure 4.8. Ratio values for wet snow mainly stayed negative while some are mixed with non-wet snow near 0dB. Some of the wet snow pixels do not show decreased backscatter from non-wet snow, and Logistic Regression and SVM successfully identified these pixels.

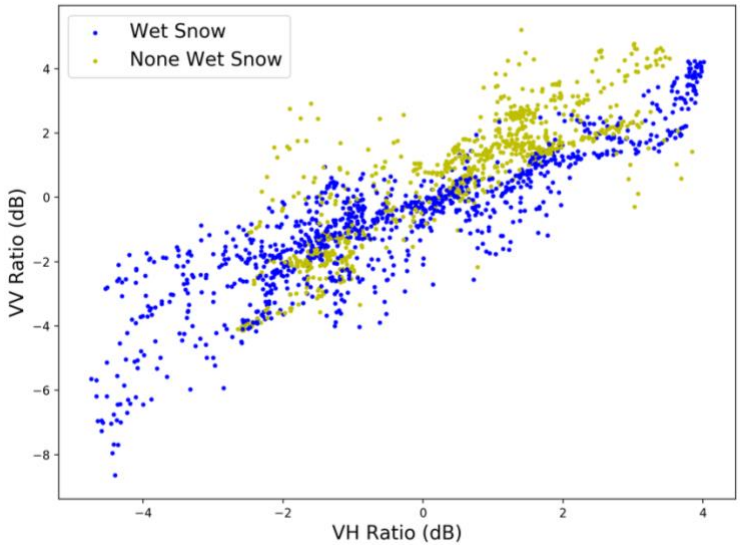

(a) Distribution of Ratio Values

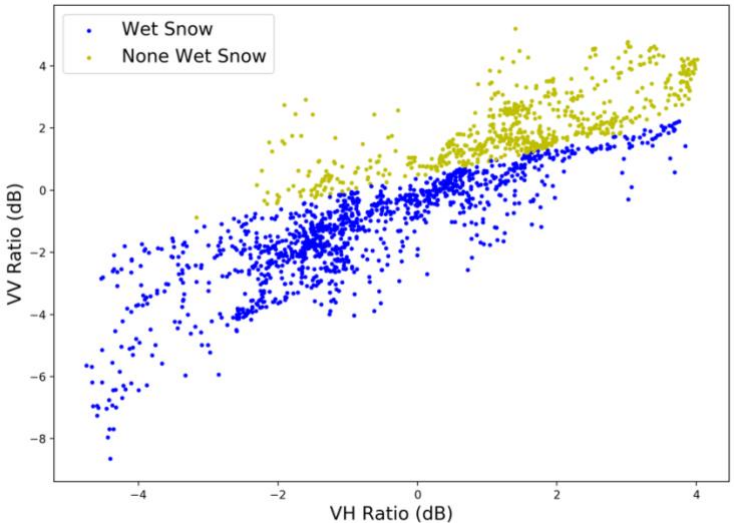

(b) Distribution of Ratio Values from Logistic Regression

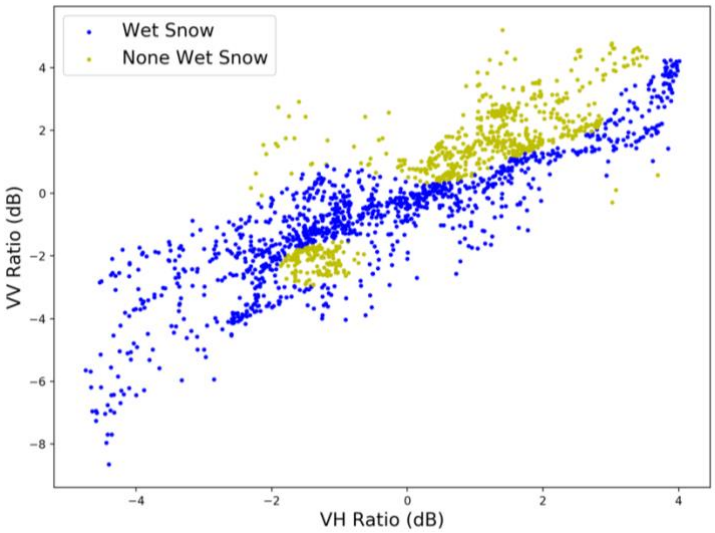

(c) Distribution of Ratio Values from SVM Classification

Figure 4.8 Distribution of Ratio Values

Figure 4.9 presents the binary snow maps from the classifications and thresholds. It can be observed that the results from SVM and logistic regression show similar patterns with the threshold approach of Nagler *et al.* (2016) and SNODAS Snowpack Temperature maps. However, on January 15, the classified results identified more wet snow in the southern areas where SNODAS indicated no snow existence.

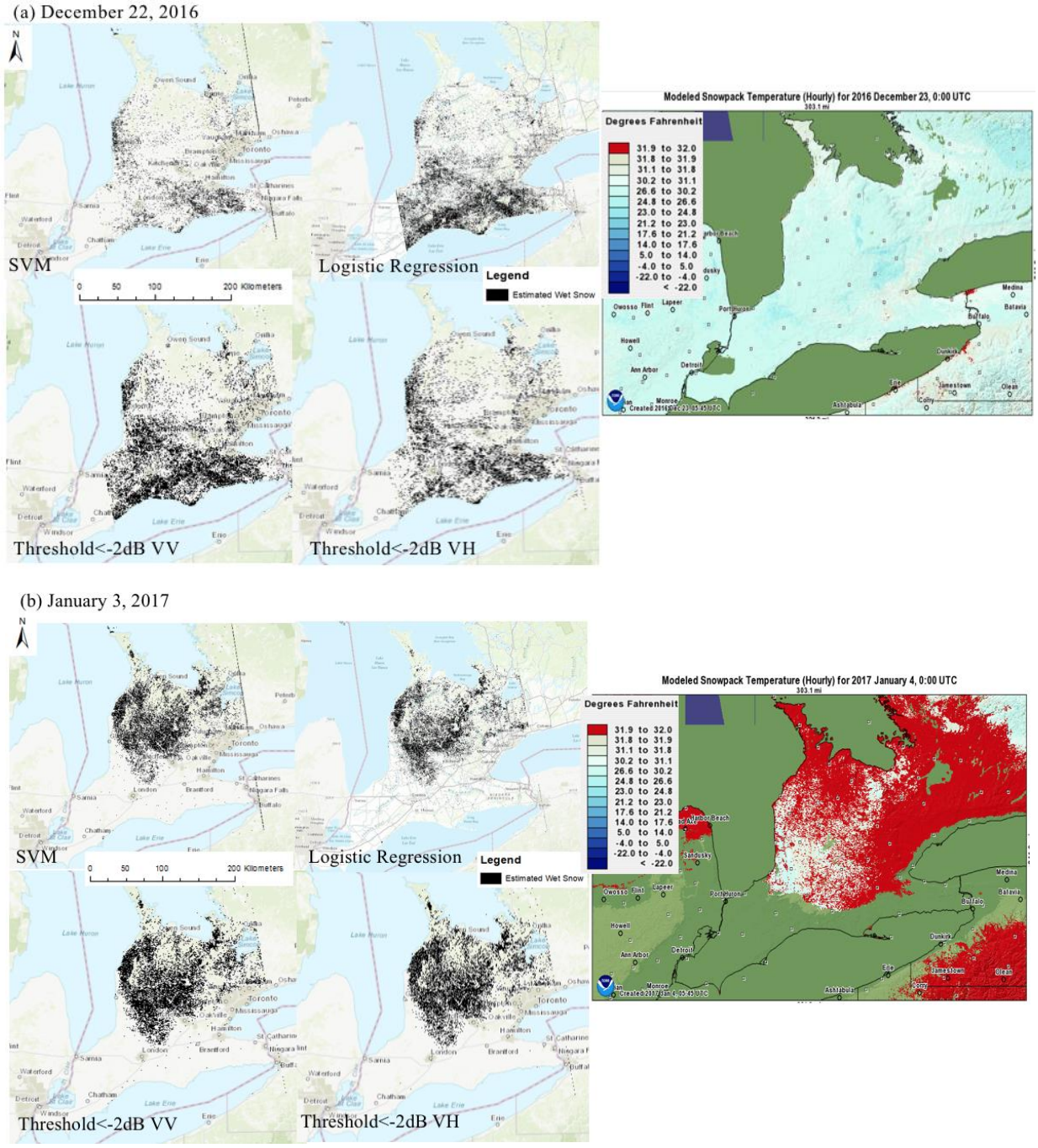

Figure 4.9 Binary Snow Maps from SVM and Logistic Regression

(c) January 15, 2017

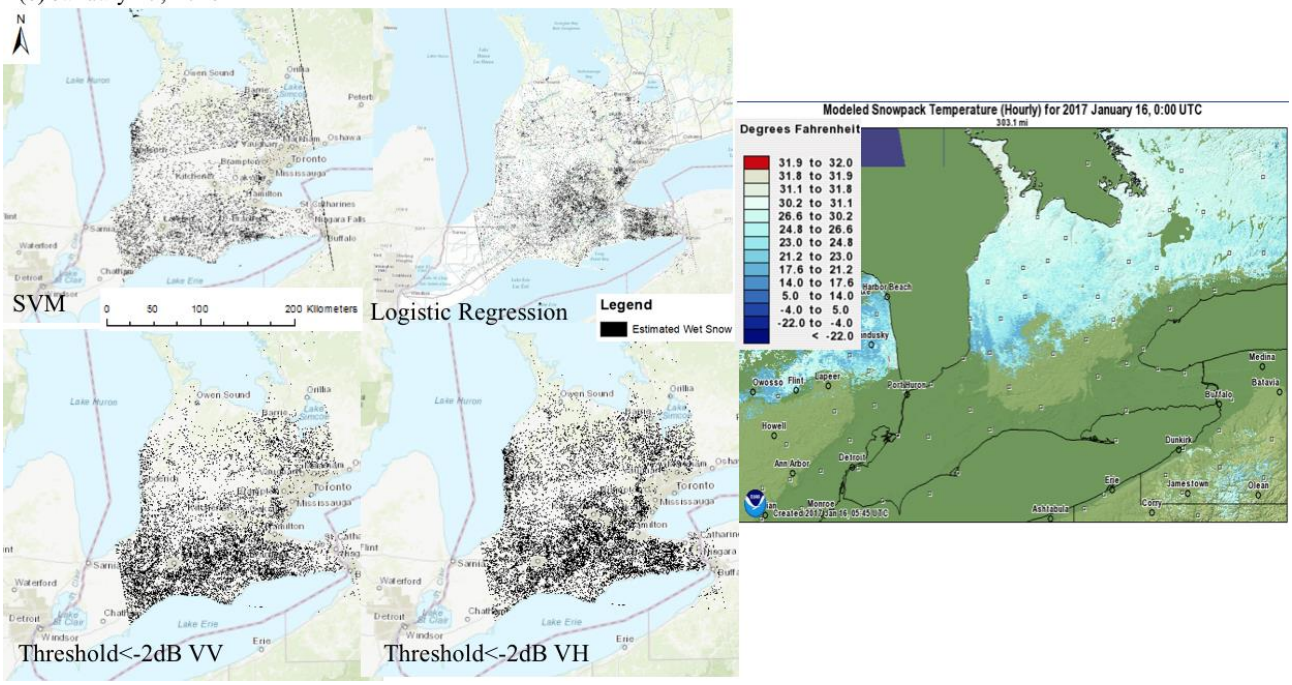

(d) February 20, 2017

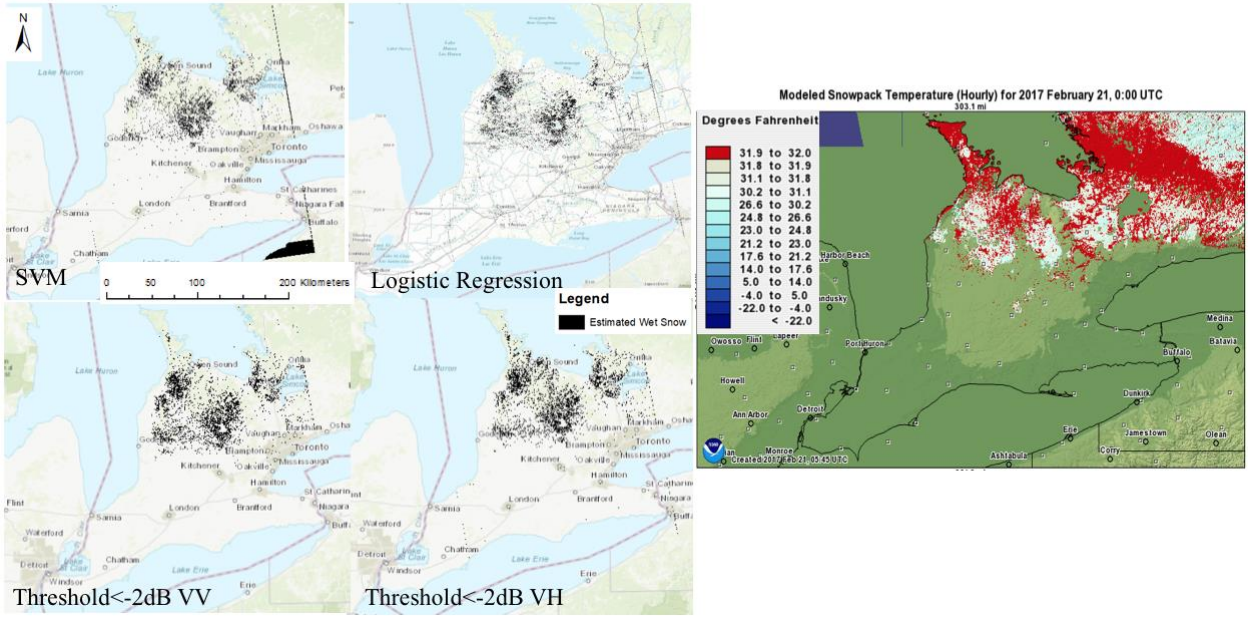

Figure 4.9 (cont.)

(e) April 9, 2017

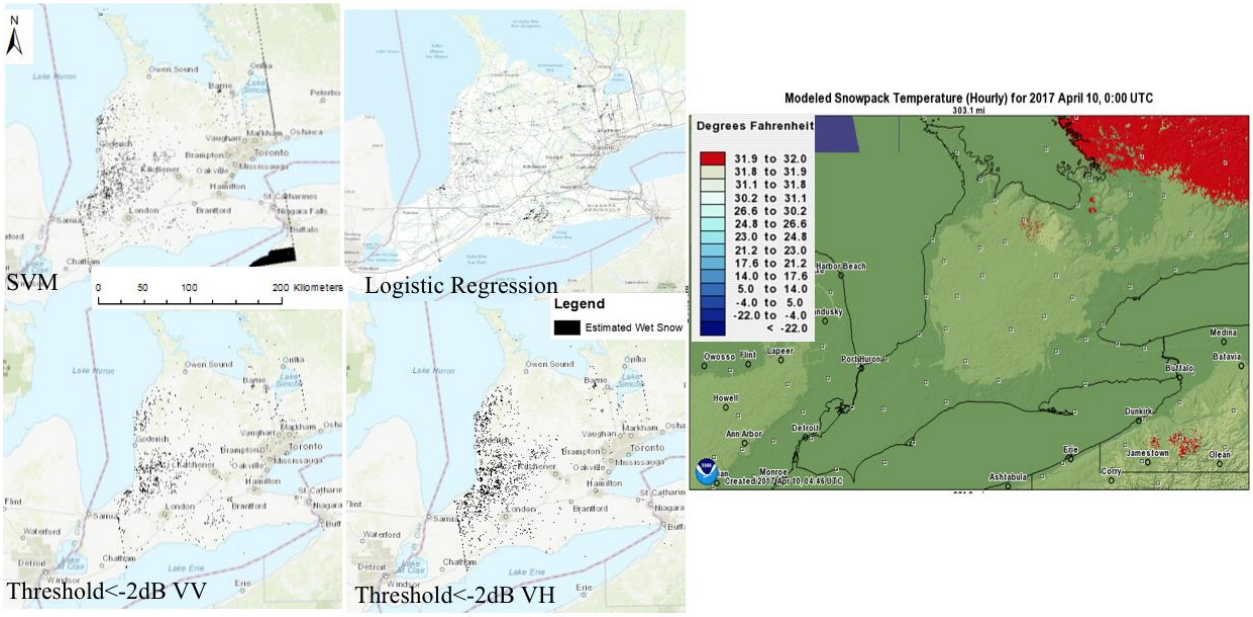

Figure 4.9 (cont.)

Chapter 5 Discussion

In this thesis an evaluation of Sentinel-1A SAR estimates of wet snow was conducted to test the Nagler *et al.* (2016) approach and to determine whether advanced classification approaches (logistic regression and SVM) provided increased performance over the Nagler *et al.* (2016) approach. Both thresholding and classification approaches used a backscatter ratio as part of the approach, so before comparisons were done, several factors were explored to determine their influence on the backscatter ratio behavior of wet snow.

5.1 Backscatter Behavior of Wet Snow

Generally, backscatter of wet snow under C-band SAR shows a significant decrease from that of non-wet snow because of the existence of liquid water. A seasonal dry snowpack is generally transparent to C-band SAR observations, so that the backscatter from dry snow merely consists of the surface scattering from the subnivean surfaces including soil and buried vegetation. Therefore, at C-band, dry snow cannot easily be differentiated from bare ground. The presence of liquid water content increases the dielectric contrast between the snow and air boundary, surface scattering from the air and wet snow interface and volume scattering contribute to the backscatter of wet snow. Furthermore, effects from terrain, incidence angle, polarization and meteorological factors can influence the backscatter ratio response. These factors are discussed below.

5.1.1 Terrain

Steep mountainous terrain typically cause layover and foreshortening image effects due to the side-looking viewing geometry of SAR, which will result in geometrical distortions of backscatter values (Nagler &Rott, 2000). Therefore, researchers usually conduct terrain correction and generate maps of layover, radar shadow and local incidence angles to refine the wet snow mapping results (Nagler &Rott, 2000; Nagler *et al.*, 2016). From the comparisons of ratios before and after terrain correction in Figure 4.3 and Table 4.1, it can be observed that the impact of terrain relief in geometrical distortion was limited and did not affect backscatter values since the ratios after terrain correction remained similar with high correlation and relatively small standard error compared with uncorrected ratios. It can be speculated that the change detection method could be applicable to other low relief terrain regions.

5.1.2 Incidence Angle

Previous studies concluded that for co-polarized images, when the incidence angle is greater than 20°, the backscatter of wet snow would significantly decrease, but surface scattering will still be dominant at around 23°, so that the backscatter will be greatly influenced by the surface properties (Baghdadi *et al.*, 1996). If the wet snow surface is rough, it might not be able to be distinguished from dry snow/bare ground (Magagi & Bernier, 2003). When the incidence angle increases, the influences from surface scattering will decrease, which therefore will make the differences between wet snow and dry snow clearer. Magagi and Bernier (2003) evaluated the optimal conditions for wet snow mapping with RADARSAT HH data using different modes with different ranges of incidence angles. The mode with incidence angle of around 45° was deemed most suitable for very wet snow detection with a rough surface, whilst the mode with an incidence angle around 25° could only identify the wet snow with low liquid water content and smooth surface.

From the boxplots in Figure 4.3, the relationship between local incidence angle and backscatter ratio is not strong because of the limited datasets and various factors influencing backscatter behaviors. However, from the plot of HH ratios, it can be observed that the ratios in small incidence angles were high, and the wet snow did not show explicit decreased backscatter from non-wet snow. With the increase of incidence angles, the ratio values tended to stay negative near incidence angle of 30°. From the summary of ratios values from 2014-2015 winter, it can be observed that some of the values were positive for ROIs with potential wet snow, which might be caused by the high backscatter from the wet snow due to low incidence angles. It can further indicate that the separability between wet snow and non-wet snow was not clear under low incidence angles. For example, on November 22, ROI 1 obtained positive high values of HH ratios with small incidence angles of around 26° and did not demonstrate low backscatter from wet snow, but ROI 13 and 14 successfully identified wet snow of decreased backscatter with a moderate incidence angle of around 35°. Similarly, the images of 2015-2016 from HH polarizations were also acquired with low incidence angles, and the ratios were not explicitly decreased for areas with wet snow. On the other hand, for 2016-2017 winter, the ratios generally stayed negative because of decreased backscatter of wet snow with high ranges of incidence angles. In summary, HH polarized images were greatly influenced by small incidence angles and cannot easily differentiate wet snow from non-wet snow targets.

5.1.3 Polarization

Studies have demonstrated that the influences of incidence angles are important for co-polarizations, while cross-polarizations are not very sensitive to the angular response (Nagler *et al.*, 2016). As the backscatter of the cross polarization merely comes from volume scattering, it should not be greatly influenced by low incidence angles, whereas the backscatter of wet snow from the co-polarization might be influenced. From Figure 4.3, the boxplot from HH polarized images tended to show a decrease of the ratio values from positive to negative towards the increase of incidence angles, but the ratio values from HV images generally remained negative. The VV and VH images did not show obvious patterns of change related to incidence angles because the incidence angles were relatively high. The different influences of incidence angle on polarizations can be observed for HV image of ROI 9 on November 22, 2014, which showed a low ratio value of -2.49 dB and clearly indicated the existence of wet snow, while HH image only showed a difference of -0.11 dB because of the small incidence angle of 26°. On January 25, 2016, ROI 1 of southern part also showed smaller influences from incidence angle on HV image than that on HH image. In summary, the cross-polarized images were less sensitive to small incidence angles, and with high range of incidence angles, co- and cross-polarized images showed generally clear patterns of wet snow from non-wet snow.

5.1.4 Meteorological Factors

The backscatter behavior of the wet snow can be influenced by temperature, snow depth and specific weather events. From the plots of the relationship between snow depth and temperature with classified wet snow and non-wet snow of different thresholds in Figure 4.5, it can be observed that with increasing thresholds, the number of misclassified wet snow pixels decreased, and they were mainly located at the boundary of melting snow and shallow snow depth. When the snow depth was shallow (smaller than 5cm), the backscatter of wet snow did not show an explicit decrease. On the other hand, when the air temperature approaches freezing point, it can be difficult to determine the existence of wet snow as the snowpack might not start to melt straight away, especially when the snow depth is thick. For example, on December 22, 2016, the thick snowpack of 20 cm from ROI 1 in northern area did not show small ratio values even with -0.1°C, which is close to the melting point of snow.

Moreover, with temperatures above freezing point, the very shallow snow (<5cm) might have very rough surface with a similar backscatter with bare ground and make the identification of wet snow difficult. For example, on November 22, 2014, ROI 7 with a local incidence angle of around 21° did not show the decreased backscatter of wet snow. The ratio of HV image was lower than that of HH image, but still cannot distinguish wet snow from dry snow with significant differences, which might be caused by the rough surface with a shallow snow depth of 2cm. The influence of snow depth can also be observed on December 28, 2014, the ROI 14 obtained high ratios from both polarizations with existence of trace snow under a moderate local incidence angle of around 35°, which should be in the optimum range of incidence angle for wet snow mapping. On January 3, 2017, the snow depths for ROI 1, 2 and 3 in southern part were recorded as "trace" from the weather station and the ratios from both VV and VH did not show differences of wet snow from the reference, whereas for the ROIs with snow depth around 15cm, the ratios were lower than -2dB. Additionally, there was freezing rain occurred on March 25, 2016, when the surface of snowpack might be rough, and it might be frozen with the near freezing temperature, so that the backscatter values were relatively high and did not indicate the existence of wet snow. In summary, the high ratio values indicated that the air temperature close to freezing point could add uncertainties of identifying the snowpack conditions. Snow depth was also found to influence the melt process and the snow surface properties, which therefore can influence the backscatter behavior of wet snow and make the identification of wet snow difficult.

The best approach to monitoring wet snow is likely using cross-polarized backscatter, which is shown to be least influenced by incidence angles. Moreover, images from 2016 to 2017 with VV and VH polarizations are recommended for wet snow mapping.

5.2 Threshold Assessment

5.2.1 -2dB Threshold

Due to the imbalanced number of ROIs with wet and non-wet snow, especially in 2015 to 2016, the accuracy metrics cannot represent the full performance of the threshold. Therefore, even though the overall accuracies of images from 2014 to2016 were relatively higher than that from 2016 to 2017, the precisions and recall data indicated that the success of identifying wet snow from 2014 to 2015 and 2015 to 2016 winter was relatively lower than that of 2016 to 2017 winter. The incidence angles for the first two years were relatively low, and therefore influenced the

separability between wet and dry snow. As 2016 to 2017 images were obtained with high incidence angles, both the precision and recall for VV and VH were relatively higher. Moreover, in 2014 to 2015, cross-polarization estimates shared similar accuracies with co-polarization estimates, while for the next two years, cross-polarization showed higher accuracy than co-polarization. Overall, most of the non-wet snow surfaces were successfully classified, while some of the wet snow areas were not identified successfully due to meteorological factors stated in 5.1. Moreover, the 2015 to 2016 datasets were not representative because there were only one or two ROIs that contained wet snow for each day and the temperature was just below freezing point, which contained uncertainties for the judgement. From the accuracy assessment on 2014 to 2016 images, it is suggested that the 2016 to 2017 datasets with higher incidence angles are more suitable for wet snow mapping using the standard Nagler *et al.* (2016) thresholding approach.

5.2.2 Necessity of Adjusting Threshold

For HH/HV images, from the sensitivity analysis of thresholds, with increasing recall but decreasing precision, it can be seen that the success for identifying wet snow increased with the higher threshold, but it was at the expense of increased misclassifications of non-wet snow. From Table 4.2 and Figure 4.7, it was indicated a higher threshold for VV/VH images, as both the precision and recall increase with higher accuracy. However, from the scatter plot in Figure 4.8 (a), it can be seen that there were a large group of mixed wet and non-wet snow in the range of 0 to -2dB for both polarizations, and for the values less than -2dB can be merely identified as wet snow. Therefore, among the test thresholds, -2dB is still considered to be a suitable choice for wet snow detection rather than the other thresholds. This adds weight to the approach devised for alpine terrain by Nagler *et al.* (2016).

5.3 Classification assessment

The classification development used the 2016-2017 datasets only for which the influences of incidence angle on backscatter responses were minimal. From the scatter plot of the distribution of ratio values in Figure 4.8(a), when the ratios were less than -2dB for both co- and cross-polarization, the pixels were all true wet snow pixels. For ratios in the range of around -2 to 0 dB for VH polarization and less than -2dB of for VV polarization, there was a clustering of non-wet snow pixels. This also corresponded to the sensitivity analysis of threshold (see Table 4.2) where VH obtained higher precisions and recalls than VV for different thresholds. Logistic regression

had a higher accuracy than the threshold method of Nagler *et al*. (2016) (Table 4.3) because it classified the pixels in the 0 to -2 dB range as wet snow, whereas SVM successfully identified the pixels as non-wet snow, resulting in the SVM approach giving the highest accuracies among the three methods. Non-wet snow pixels were mainly identified above the 0 dB ratio value, but some wet snow pixels were also found in this range, where the ratios might be influenced by the temperature and snow depth. These wet snow pixels with high ratio values might be greatly influenced by meteorological factors, which matched with misclassified wet snow on the boundary of shallow snow depth in Figure 4.5 even with high threshold of -0.5dB. As logistic regression still lost some of the wet snow pixels with positive ratios, SVM classified a large group of wet snow, which result in a more accurate identification. When applying on the whole scene, the amount of non- and wet snow was imbalanced, and to reduce the false positive rate, higher thresholds of probability were used. The recall of logistic regression was reduced by a large amount with a decrease in the false positive rate, while the recall of SVM generally remained constant indicating a superior performance of SVM. The classification results in Figure 4.9 illustrated the possibility of using classification methods on the whole scene although it should be noted that there were no ground reference observations of the whole scene to evaluate these results. Moreover, as the classifiers were devised for an agricultural land class, and other land cover types might control the wet snow phase development differently, the classifiers might not be able to provide an accurate mapping of wet snow for the whole scene. Nevertheless, classification methods, especially SVM, indicated an improved performance relative to the threshold method on account of the non-linear estimation characteristics of the classifiers. The threshold approach, however, was only able to provide a linear separation of wet snow and non-wet snow and is less able to account for non-linear cases of wet snow presence. However, the results contained uncertainties, which existed in the datasets and processes and will be discussed in 5.4.

5.4 Uncertainties

Even though many influencing factors are explained in 5.1, there were residual influences from the datasets and methods used in this study.

5.4.1 Limited Ground Reference

For this study, there were missing data in the meteorological record, which added uncertainty to the interpretation of wet snow pixels. Also, there were several days when air temperatures were

close to the freezing point, which made the judgement of wet snow uncertain since they could have been slightly above or slightly below freezing. As the weather stations measured the air temperature, it was hard to know the conditions inside the snowpack and to determine if the snow started to melt. Direct and diffuse solar heating processes are capable of warming the snowpack even when measured air temperatures are below freezing (Dingman, 2015). Some of the snow depth measurements were missing, and the existence of snow was determined using MODIS snow cover data due to the lack of high resolution optical images. As MODIS data was in a low resolution of 500m, it might not be able to correctly characterize the existence of snow for places around the immediate vicinity of the weather stations. Another uncertainty from the temperature is the snow wetness. Guneriussen (1997) found that even a very low snow liquid water content will decrease the volume scattering. When the liquid water content is high in the snowpack, the surface would be rougher, and rough wet snow would be hard to differentiate from non-wet snow. Magagi and Bernier (2003) also observed that the snow liquid water content decreased the differences between wet snow and non-wet snow. For our study, due to the lack of in situ ground reference snow data, the snow wetness was unknown and so it was difficult to generate quantitative relationships between the snow surface properties and the backscatter behaviours. Therefore, since snow surface roughness was essentially unknown, its influence on this study remains unknown. Moreover, uncertainties of the ground reference data added uncertainties to the classifications potentially due to labelling uncertainty. Generally, from Figure 4.9 the classified wet snow maps aligned with SNODAS Snowpack Temperature maps with similar patterns. However, the SNODAS Snowpack Temperature maps were modeled, where there might be overestimated or underestimated temperatures, so that the wet snow maps from the classifiers were unable to be accurately compared and remained uncertainties of the performance.

5.4.2 Limited ROIs

The ROIs were only selected over agricultural land where the weather station sites were located. Snow accumulation on different land cover types may produce different backscatter features on account of the fact that different boundary conditions will produce different thermodynamic processes that result in more or less complex snowpack physical properties (including melt regimes). Whilst the three years of datasets used showed promising results, further years will be needed to demonstrate clear patterns of backscatter behavior from wet snow. Meanwhile, the

agricultural land consists of different types of agriculture plants, which might influence the wet snow conditions.

5.4.3 Residual Speckle Noise

Efforts were made to reduce speckle noise through the use of single and multi-temporal speckle filters. Ultimately, however, the speckle noise reduction does not completely remove the noise (Lee et al.,2006). For the wet snow mapping procedures, because the process was pixel-based, some of the pixels might have biased values caused by residual speckle noise, for which the influences remained unknown.

5.4.4 Reference Image

For the reference images used for each winter period from the end of October to the following year's April, images from days without potential wet snow were averaged. However, the reference images might contain rainy days, which might make the average low and reduce the differences with wet snow. A good strategy for the future, therefore, would be to continually expand the reference image by adding suitable images without wet snow to provide more general backscatter features.

5.4.5 Imbalanced Data

As mentioned previously, the classifiers were built on agricultural land and balanced as a dataset containing wet and non-wet snow. However, the whole scene might have many more non-wet snow than wet snow pixels. Even though the threshold was tuned based on the statistics from cross-evaluation, the real condition for the whole scene can be different and the false positive rate could vary for different scenes. Therefore, imbalanced data added uncertainty to the application of the classification models.

Despite these various limitations, the analysis indicates that Sentinel-1A datasets can be used to map wet snow in Southern Ontario with both change detection method and advanced classifications.

5.5 Future work

As one of the biggest limitations was the accuracy and accessibility of the ground reference data, future work should include field work to obtain *in situ* datasets, such as snow temperature and snow depth to increase more confidence for wet snow judgment. Additionally, more parameters

of snow properties, such as snow wetness and surface roughness can be collected from field work and can provide more valid support for the analysis of backscatter behaviors. This study only involved agricultural land for assessing the wet snow classification method, while different land cover should be analyzed separately to test the backscatter responses in the future. By using the ground reference identified areas from different land cover types to label datasets, more robust classifiers can be built. Future studies should add the following years' images to further validate the usefulness of VV and VH images from IW mode. As discussed above, this study used the same threshold applying on images from both polarizations, where the ratios were in different ranges for different polarizations, so it is suggested to involve weighted combinations of values from different polarizations. Nagler *et al.* (2016) combined the two polarizations based on the relationship with local incidence angle, and future work for Southern Ontario will need further analysis on the relationships of ratios and other parameters. Moreover, the features used in the classification of this study were the ratio images, and the information might be reduced from the original backscatter images. Therefore, involving the original backscatter images and more available datasets as input features might also increase the accuracy of classification. With the availability of full-polarized SAR data, polarimetric images will also be able to provide more information of snow properties, which therefore can help develop new classification methods.

5.6 Main Findings

This study has assessed the applicability of the change detection method on agricultural land in Southern Ontario and compared with classification methods. It has been noticed that the HH HV images used in this study were in low incidence angles, which may influence the separability of wet snow and non-wet snow. Therefore, for Sentinel-1A images, IW VV&VH images are more recommended for wet snow mapping due to the high range of incidence angles. Images of both cross- and co-polarization should be used together to provide more information. The change detection method is robust to identifying wet snow with decreased backscatter, however, due to the influences of different factors, threshold cannot classify all the wet snow by the simple linear boundary. Thus, the logistic regression and SVM classifications applied in this study have shown higher accuracies and indicated a new method to identify wet snow for this study area.

Chapter 6 Conclusion

Given that wet snow can be an indicator of climate change and has important hydrological and ecological influences, monitoring seasonal snow cover changes has been an important topic for a long while. As SAR has the capabilities of working under all weather conditions with whole day image acquisition and providing images with high resolution, it has shown great advantages over optical systems to monitor the Earth surface. C-band has been found to be sensitive to wet snow, which can observe differences in backscatter of wet snow from non-wet snow. Researchers have developed a robust change detection method to identify wet snow with C-band SAR images (Nagler *et al*., 2016). With improved data availabilities, multi-temporal and multi-polarized images rather than single polarized images were widely used for wet snow mapping to provide more accurate results. Sentinel satellite missions have been proven to provide a large range of applications with easy accessibility and helpful user community. Sentinel-1A offers dual-polarized C-band SAR images and were used in this study for wet snow mapping. Previous studies mainly focused on mountainous areas; however, this study chose Southern Ontario as study area, which is generally flat and is a combination of developed, agricultural and natural land. This study aimed to assess the applicability of the conventional method to identify wet snow in a non-mountainous area and to compare with classification methods.

In this study, three years (2014-2017) of Sentinel-1A images were used. Due to the data availability for Southern Ontario, the first two years' images were obtained in EW model, where HH and HV polarized images were available, while VV and VH images from IW mode were used for 2016-2017 winter. Since there were no studies on wet snow mapping for this study area, change detection with a conventional threshold of -2dB was applied first and followed by a sensitivity analysis of different thresholds. ROIs of agricultural land were collected to examine the factors influencing the backscatter behaviors of wet snow. A comparison between the thresholding results and ground reference data, which were generated from MODIS and meteorological datasets were conducted for each winter period with each polarization. Four other thresholds were tested in the sensitivity analysis, but no obvious accuracy improvement was observed. Logistic regression and SVM classifications were applied to compare with the threshold method in order to improve the performance of wet snow mapping. It has been noticed that the HH and HV images from EW mode were in low incidence angles, and the backscatter of wet snow was greatly influenced. Therefore,

only VV and VH ratio images from 2016 to 2017were used in the logistic regression and SVM classifications. This study has proved the applicability of change detection method in a flat area with various factors influencing the backscatter, and a threshold of -2dB was reasonable. However, classification methods resulted in better performance and accuracies by identifying non-linear characteristics of the dataset rather than the thresholding method with simple linear boundary.

Sources of uncertainties of this study stemmed from the availability and accuracy of data. Meteorological and MODIS data involved uncertainties to identify the existence of wet snow. Some of the backscatter behavior were difficult to explain due to the lack of ground reference to support. As the images only covered three years, the sample sizes for ROIs were limited. Therefore, it is suggested to conduct field work to collect in situ data to support classifications. Except for using air temperature, snow temperature can be also helpful to identify the existence of wet snow. Other snow properties such as surface roughness and wetness can also help better understand the backscatter behaviors. As this study only involved agricultural land, the method remained unknown for different land cover types and future work should test on different land cover. With more availability of data, such as following years' images and ground reference datasets, the classification methods can be more robust with more features and more reliable labelled dataset. Full-polarized SAR images and InSAR images will also be able to provide more information of snow properties, which therefore can help develop new classification methods.

References

Akitaya, E. (1974). Studies on depth hoar. *Institute of Low Temperature Science*, Hokkaido University.

Armstrong, R. L., & Brun, E. (2008). *Snow and climate: physical processes, surface energy exchange and modeling*. Cambridge University Press.

Baghdadi, N., Livingstone, C. E., & Bernier, M. (1998). Airborne C-band SAR measurements of wet snow-covered areas. *IEEE transactions on geoscience and remote sensing*, 36(6), 1977-1981.

Baraldi, A., & Parmiggiani, F. (1995). A refined Gamma MAP SAR speckle filter with improved geometrical adaptivity. *IEEE Transactions on Geoscience and Remote Sensing*, *33*(5), 1245-1257.

Bernier, P. Y. (1987). Microwave remote sensing of snowpack properties: potential and limitations. *Hydrology Research*, *18*(1), 1-20.

Besic, N., Vasile, G., Dedieu, J. P., Chanussot, J., & Stankovic, S. (2015). Stochastic Approach in Wet Snow Detection Using Multitemporal SAR Data. *IEEE Geoscience and Remote Sensing Letters*, 12(2), 244-248.

Bishop, M. P., Björnsson, H., Haeberli, W., Oerlemans, J., Shroder, J. F., & Tranter, M. (2011). *Encyclopedia of snow, ice and glaciers*. V. P. Singh, P. Singh, & U. K. Haritashya (Eds.). Springer Science & Business Media.

Brown, R. D., & Mote, P. W. (2009). The response of northern hemisphere snow cover to a changing climate. *Journal of Climate*, *22*(8), 2124-2145.

Chang, A. T. C., Foster, J. L., Hall, D. K., Rango, A., & Hartline, B. K. (1982). Snow water equivalent estimation by microwave radiometry. *Cold Regions Science and Technology*, *5*(3), 259-267.

Colbeck, S. C. (1983). Theory of metamorphism of dry snow. *Journal of Geophysical Research: Oceans*, *88*(C9), 5475-5482.

Congalton, R.G., 1991. A review of assessing the accuracy of classifications of remotely sensed data. *Remote Sensing of Environment*, 37(1), pp.35–46.

Derksen, C., & Brown, R. (2012). Spring snow cover extent reductions in the 2008–2012 period exceeding climate model projections. *Geophysical Research Letters*, *39*(19).

Déry, S. J., & Brown, R. D. (2007). Recent Northern Hemisphere snow cover extent trends and implications for the snow-albedo feedback. *Geophysical Research Letters*, *34*(22).

De Zan, F., & Guarnieri, A. M. (2006). TOPSAR: Terrain observation by progressive scans. *IEEE Transactions on Geoscience and Remote Sensing*, 44(9), 2352-2360.

Dingman, S. L. (2015). *Physical hydrology*. Waveland press.

Eineder, M. and Bamler, R., 2014. SAR Imaging. Lecture at SAR-EDU, November 7, 2014. Available at: <https://saredu.dlr.de/unit/SAR_imaging>

European Space Agency. (2016). *Sentinel-1 SAR user guides*. Retrieved from https://sentinel.esa.int/web/sentinel/user-guides/

Essery, R., & Pomeroy, J. (2004). Vegetation and topographic control of wind-blown snow distributions in distributed and aggregated simulations for an Arctic tundra basin. *Journal of Hydrometeorology*, *5*(5), 735-744.

Etchevers, P., Martin, E., Brown, R., Fierz, C., Lejeune, Y., Bazile, E., ... & Gusev, Y. (2004). Validation of the energy budget of an alpine snowpack simulated by several snow models (SnowMIP project). *Annals of Glaciology*, *38*(1), 150-158.

Evans S. 1965. The dielectric properties of ice and snow – a review.

Fawcett, T. (2006). An introduction to ROC analysis. *Pattern recognition letters*, 27(8), 861-874.

Frost, V. S., Stiles, J. A., Shanmugan, K. S., & Holtzman, J. C. (1982). A model for radar images and its application to adaptive digital filtering of multiplicative noise. *IEEE Transactions on pattern analysis and machine intelligence*, (2), 157-166.

Gray, D. M., & Male, D. H. (Eds.). (1981). *Handbook of snow: principles, processes, management & use*. Pergamon Press.

Guneriussen, T. (1998). *Snow characteristics in mountainous areas as observed with synthetic aperture radar (SAR) instruments*.

Haefner, H., & Piesbergen, J. (1997). High alpine snow cover monitoring using ERS-1 SAR and Landsat TM data. *IAHS Publications-Series of Proceedings and Reports-Intern Assoc Hydrological Sciences*, *242*, 113-118

Hall, D. K., Foster, J. L., Verbyla, D. L., Klein, A. G., & Benson, C. S. (1998). Assessment of snow-cover mapping accuracy in a variety of vegetation-cover densities in central Alaska. *Remote sensing of Environment*, *66*(2), 129-137.

Hallikainen M. 1977. Dielectric properties of sea ice at microwave frequencies. *NASA STI/Recon Technical Report N*. 781:11293.

He, G., Xiao, P., Feng, X., Zhang, X., Wang, Z., & Chen, N. (2015). Extracting Snow Cover in Mountain Areas Based on SAR and Optical Data. *IEEE Geoscience and Remote Sensing Letters*, 12(5), 1136-1140.

Huang, L., Li, Z., Tian, B. S., Chen, Q., Liu, J. L., & Zhang, R. (2011). Classification and snow line detection for glacial areas using the polarimetric SAR image. *Remote Sensing of Environment*, 115(7), 1721-1732.

Ko, S. J., & Lee, Y. H. (1991). Center weighted median filters and their applications to image enhancement. *IEEE transactions on circuits and systems*, *38*(9), 984-993.

Kumai, M. (1961). Snow crystals and the identification of the nuclei in the northern United States of America. *Journal of Meteorology*, *18*(2), 139-150.

Libbrecht, K. G. (2005). The physics of snow crystals. *Reports on progress in physics*, *68*(4), 855.

Lee, J. S., Grunes, M. R., Schuler, D. L., Pottier, E., & Ferro-Famil, L. (2006). Scattering-model-based speckle filtering of polarimetric SAR data. *IEEE Transactions on Geoscience and Remote Sensing*, *44*(1), 176-187.

Lopes, A., Touzi, R., & Nezry, E. (1990). Adaptive speckle filters and scene heterogeneity. *IEEE transactions on Geoscience and Remote Sensing*, *28*(6), 992-1000.

Magagi, R., & Bernier, M. (2003). Optimal conditions for wet snow detection using RADARSAT SAR data. Remote Sensing of Environment, 84(2), 221-233.

Mätzler, C., & Schanda, E. (1984). Snow mapping with active microwave sensors. *Remote Sensing*, 5(2), 409-422.

McCloskey, D. N., & Ziliak, S. T. (1996). The standard error of regressions. *Journal of economic literature*, 34(1), 97-114.

McClung, D., & Schaerer, P. A. (2006). *The avalanche handbook*. The Mountaineers Books.

Meiman, J. R. (1970). Snow accumulation related to elevation, aspect, and forest canopy. In *Snow hydrology: Proceedings. Workshop seminar on snow hydrology, Fredericton, 28-29 Feb. 1969.* (pp. 35-47).

Menard, S. (2018). *Applied logistic regression analysis* (Vol. 106). SAGE publications.

Moreira, A., 2013. Synthetic aperture radar (SAR): principles and applications. In: *4th Advanced Training Course in Land Remote Sensing*. ESA.

Mudryk, L., C. Derksen, S. Howell, F. Laliberte, C. Thackeray, R. Sospedra-Alfonso, V. Vionnet, P. Kushner, 1458 and R. Brown. 2017b. Canadian snow and sea ice trends (1981-2015) and projections (2020-2050). *The 1459 Cryosphere Discussions.*

Nagler, T., & Rott, H. (2000). Retrieval of wet snow by means of multitemporal SAR data. *IEEE Transactions on Geoscience and Remote Sensing*, *38*(2), 754-765.

Nagler, T., Rott, H., Ripper, E., Bippus, G., & Hetzenecker, M. (2016). Advancements for Snowmelt Monitoring by Means of Sentinel-1 SAR. *Remote Sensing*, *8*(4), 348.

Natural Resources of Canada. (2015, November 20). *Radar Polarimetry*. Retrieved from http://www.nrcan.gc.ca/node/9275

Park, S. E., Yamaguchi, Y., Singh, G., Yamaguchi, S., & Whitaker, A. C. (2014). Polarimetric SAR response of snow-covered area observed by multi-temporal ALOS PALSAR fully polarimetric mode. *IEEE Transactions on Geoscience and Remote Sensing*, 52(1), 329- 340.

Richards, J.A., 2009. *Remote sensing with imaging radar.* Springer Berlin Heidelberg.

Rondeau-Genesse, G., Trudel, M., & Leconte, R. (2016). Monitoring snow wetness in an Alpine Basin using combined C-band SAR and MODIS data. *Remote Sensing of Environment*, *183*, 304-317.

Rosenfeld, D. (2000). Suppression of rain and snow by urban and industrial air pollution. *Science*, *287*(5459), 1793-1796.

Rott, H., & Nagler, T. (1994). Capabilities of ERS-1 SAR for snow and glacier monitoring in alpine areas. *European Space Agency Publications ESA Sp*, *361*, 965-965.

Rott H, Mätzler C, Strobl D, BruzziS, Lenhart KB. (1988). Study on SAR land applications for snow and glacier monitoring. *ESA Contract Report* 6618 185 IFIFL (SC)

Rott, H., Yueh, S. H., Cline, D. W., Duguay, C., Essery, R., Haas, C., ... & Nagler, T. (2010). Cold regions hydrology high-resolution observatory for snow and cold land processes. *Proceedings of the IEEE*, *98*(5), 752-765.

Royer, A., Goïta, K., Kohn, J., & De Sève, D. (2010). Monitoring dry, wet, and no-snow conditions from microwave satellite observations. *IEEE Geoscience and Remote Sensing Letters*, *7*(4), 670-674.

Schanda, E., Matzler, C., & Kunzi, K. (1983). Microwave remote sensing of snow cover. *International Journal of Remote Sensing*, *4*(1), 149-158.

Shi, J. ,& Dozier, J (1995). Inferring snow wetness using C-band data from SIR-C's polarimetric synthetic aperture radar. *IEEE Trans. Geosci. Remote Sens*, 33, 905–914

Shi, J., & Dozier, J. (1997). Mapping seasonal snow with SIR-C/X-SAR in mountainous areas. *Remote Sensing of Environment*, 59(2), 294-307.

Solberg, R., Amlien, J., Koren, H., Eikvil, L., Malnes, E., & Storvold, R. (2004). Multi-sensor and time-series approaches for monitoring of snow parameters. In *Geoscience and Remote Sensing Symposium, 2004. IGARSS'04. Proceedings. 2004 IEEE International* (Vol. 3, pp. 1661-1666). IEEE.

Sommerfeld, R. A., & LaChapelle, E. (1970). The classification of snow metamorphism. *Journal of Glaciology*, *9*(55), 3-18.

Stiles, W. H., & Ulaby, F. T. (1981). *Dielectric properties of snow.*

Strozzi, T., Wiesmann, A., & Mätzler, C. (1997). Active microwave signatures of snow covers at 5.3 and 35 GHz. *Radio Science*, 32(2), 479-495.

Sturm, M., Holmgren, J., & Liston, G. E. (1995). A seasonal snow cover classification system for local to global applications. *Journal of Climate*, 8(5), 1261-1283.

Sun, Y., Wong, A. K., & Kamel, M. S. (2009). Classification of imbalanced data: A review. *International Journal of Pattern Recognition and Artificial Intelligence*, 23(04), 687-719.

Teskey, B. J. (2012). *Tree fruit production*. Springer Science & Business Media.

Teubner, I. E., Haimberger, L., & Hantel, M. (2015). Estimating snow cover duration from ground temperature. *Journal of Applied Meteorology and Climatology*, 54(5).

Ulaby, F. T., Long, D. G., Blackwell, W. J., Elachi, C., Fung, A. K., Ruf, C., ... & Van Zyl, J. (2014). *Microwave radar and radiometric remote sensing*.

Ulaby, F. T., & Stiles, W. H. (1981). Microwave response of snow. *Advances in Space Research*, 1(10), 131-149.

Ulaby, F. T., Stiles, W. H., & AbdelRazik, M. (1984). Snowcover influence on backscattering from terrain. *IEEE Transactions on geoscience and remote sensing*, (2), 126-133.

Van der Voet, P., Van Diepen, C. A., & Voshaar, J. O. (1994). Spatial interpolation of daily meteorological data. Report 53.3 *Winand Staring Centre for Integrated Land, Soil and Water Research*, 105.

Wakahama, G. (1968). The metamorphism of wet snow. *IAHS Publication*, *79*, 370-379.

Woodhouse, I. H. (2006). *Introduction to Microwave Remote Sensing.* CRC, New York.

Yu, Y., & Acton, S. T. (2002). Speckle reducing anisotropic diffusion. *IEEE Transactions on image processing*, *11*(11), 1260-1270.

Appendices

Appendix A List of Available Sentinel-1A Scenes

Product	Date	Mode	Polarization	Pass
S1A_EW_GRDM_1SDH_20141029T230729_20141029T230833_003051_0037C6_4992	2014-10-09	EW_GRDM	HH HV	Ascending
S1A_EW_GRDM_1SDH_20141110T230729_20141110T230833_003226_003B96_B2BA	2014-11-10	EW_GRDM	HH HV	Ascending
S1A_EW_GRDM_1SDH_20141122T230729_20141122T230833_003401_003F6E_DA7E	2014-11-22	EW_GRDM	HH HV	Ascending
S1A_EW_GRDM_1SDH_20141204T230728_20141204T230832_003576_004388_582A	2014-12-04	EW_GRDM	HH HV	Ascending
S1A_EW_GRDM_1SDH_20141216T230728_20141216T230832_003751_00478B_3819	2014-12-16	EW_GRDM	HH HV	Ascending
S1A_EW_GRDM_1SDH_20141228T230728_20141228T230832_003926_004B7A_B087	2014-12-28	EW_GRDM	HH HV	Ascending
S1A_EW_GRDM_1SDH_20150109T230727_20150109T230831_004101_004F70_D1CD	2015-01-09	EW_GRDM	HH HV	Ascending
S1A_EW_GRDM_1SDH_20150121T230727_20150121T230831_004276_00533B_1A2F	2015-01-21	EW_GRDM	HH HV	Ascending
S1A_EW_GRDM_1SDH_20150202T230727_20150202T230831_004451_00573C_484B	2015-02-02	EW_GRDM	HH HV	Ascending
S1A_EW_GRDM_1SDH_20150226T230726_20150226T230830_004801_005F7C_97FE	2015-02-26	EW_GRDM	HH HV	Ascending
S1A_EW_GRDM_1SDH_20150322T230727_20150322T230831_005151_0067E5_08B2	2015-03-22	EW_GRDM	HH HV	Ascending
S1A_EW_GRDM_1SDH_20150401T232341_20150401T232445_005297_006B3C_0185	2015-04-01	EW_GRDM	HH HV	Ascending
S1A_EW_GRDM_1SDH_20150415T230727_20150415T230831_005501_007069_E39B	2015-04-15	EW_GRDM	HH HV	Ascending
S1A_EW_GRDM_1SDH_20150427T230728_20150427T230832_005676_00747F_8660	2015-04-27	EW_GRDM	HH HV	Ascending
S1A_EW_GRDM_1SDH_20151021T113654_20151021T113758_008250_00B9EE_3BC4	2015-10-21	EW_GRDM	HH HV	Descending
S1A_EW_GRDM_1SDH_20151021T113758_20151021T113843_008250_00B9EE_9FB1				
S1A_EW_GRDM_1SDH_20151114T113651_20151114T113755_008600_00C348_0930	2015-11-14	EW_GRDM	HH HV	Descending
S1A_EW_GRDM_1SDH_20151114T113755_20151114T113840_008600_00C348_872E				
S1A_EW_GRDM_1SDH_20151208T113651_20151208T113755_008950_00CD2A_8F61	2015-12-08	EW_GRDM	HH HV	Descending

S1A_EW_GRDM_1SDH_20151208T113755_20151208T113840_008950_00CD2A_4097				
S1A_EW_GRDM_1SDH_20151220T113650_20151220T113754_009125_00D1F3_4849	2015-12-20	EW_GRDM	HH HV	Descending
S1A_EW_GRDM_1SDH_20151220T113754_20151220T113839_009125_00D1F3_4EC3				
S1A_EW_GRDM_1SDH_20160101T113650_20160101T113754_009300_00D6F6_1A23	2016-01-01	EW_GRDM	HH HV	Descending
S1A_EW_GRDM_1SDH_20160101T113754_20160101T113839_009300_00D6F6_F9A6				
S1A_EW_GRDM_1SDH_20160113T113649_20160113T113753_009475_00DBF4_8925	2016-01-13	EW_GRDM	HH HV	Descending
S1A_EW_GRDM_1SDH_20160113T113753_20160113T113838_009475_00DBF4_07D9				
S1A_EW_GRDM_1SDH_20160125T113649_20160125T113753_009650_00E113_44E0	2016-01-25	EW_GRDM	HH HV	Descending
S1A_EW_GRDM_1SDH_20160125T113753_20160125T113838_009650_00E113_8750				
S1A_EW_GRDM_1SDH_20160206T113649_20160206T113753_009825_00E61D_222D	2016-02-06	EW_GRDM	HH HV	Descending
S1A_EW_GRDM_1SDH_20160206T113753_20160206T113838_009825_00E61D_3382				
S1A_EW_GRDM_1SDH_20160218T113648_20160218T113753_010000_00EB48_5A73	2016-02-18	EW_GRDM	HH HV	Descending
S1A_EW_GRDM_1SDH_20160218T113753_20160218T113837_010000_00EB48_F483				
S1A_EW_GRDM_1SDH_20160301T113648_20160301T113753_010175_00F03B_4816	2016-03-01	EW_GRDM	HH HV	Descending
S1A_EW_GRDM_1SDH_20160301T113753_20160301T113838_010175_00F03B_8707				
S1A_EW_GRDM_1SDH_20160325T113649_20160325T113753_010525_00FA31_225D	2016-03-25	EW_GRDM	HH HV	Descending
S1A_EW_GRDM_1SDH_20160325T113753_20160325T113838_010525_00FA31_3420				
S1A_EW_GRDM_1SDH_20160406T113649_20160406T113754_010700_00FF4F_D5DF	2016-04-06	EW_GRDM	HH HV	Descending
S1A_EW_GRDM_1SDH_20160406T113754_20160406T113838_010700_00FF4F_CC9F				
S1A_EW_GRDM_1SDH_20160418T113650_20160418T113754_010875_010495_2718	2016-04-18	EW_GRDM	HH HV	Descending
S1A_EW_GRDM_1SDH_20160418T113754_20160418T113839_010875_010495_70E4				
S1A_EW_GRDM_1SDH_20160430T113650_20160430T113755_011050_010A16_AC05	2016-04-30	EW_GRDM	HH HV	Descending

S1A_EW_GRDM_1SDH_20160430T113755_20160430T113839_011050_010A16_E42E				
S1A_IW_GRDH_1SDV_20161023T231604_20161023T231632_013624_015D49_E820	2016-10-23	IW_GRDH	VV VH	Ascending
S1A_IW_GRDH_1SDV_20161023T231631_20161023T231658_013624_015D49_E855				
S1A_IW_GRDH_1SDV_20161104T231605_20161104T231630_013799_0162C2_078F	2016-11-04	IW_GRDH	VV VH	Ascending
S1A_IW_GRDH_1SDV_20161104T231630_20161104T231658_013799_0162C2_E2A9				
S1A_IW_GRDH_1SDV_20161116T231604_20161116T231632_013974_016830_ABAA	2016-11-16	IW_GRDH	VV VH	Ascending
S1A_IW_GRDH_1SDV_20161116T231630_20161116T231658_013974_016830_3BD4				
S1A_IW_GRDH_1SDV_20161128T231605_20161128T231630_014149_016D93_A43E	2016-11-28	IW_GRDH	VV VH	Ascending
S1A_IW_GRDH_1SDV_20161128T231630_20161128T231657_014149_016D93_5244				
S1A_IW_GRDH_1SDV_20161210T231605_20161210T231630_014324_01731F_F1F3	2016-12-10	IW_GRDH	VV VH	Ascending
S1A_IW_GRDH_1SDV_20161210T231630_20161210T231657_014324_01731F_B4AF				
S1A_IW_GRDH_1SDV_20161222T231604_20161222T231629_014499_017895_3AC1	2016-12-22	IW_GRDH	VV VH	Ascending
S1A_IW_GRDH_1SDV_20161222T231629_20161222T231657_014499_017895_320C				
S1A_IW_GRDH_1SDV_20170103T231601_20170103T231629_014674_017DEF_A981	2017-01-03	IW_GRDH	VV VH	Ascending
S1A_IW_GRDH_1SDV_20170103T231628_20170103T231655_014674_017DEF_C5F8				
S1A_IW_GRDH_1SDV_20170115T231602_20170115T231627_014849_01834F_079C	2017-01-15	IW_GRDH	VV VH	Ascending
S1A_IW_GRDH_1SDV_20170115T231627_20170115T231655_014849_01834F_8803				
S1A_IW_GRDH_1SDV_20170127T231602_20170127T231627_015024_0188B3_24E6	2017-01-27	IW_GRDH	VV VH	Ascending
S1A_IW_GRDH_1SDV_20170127T231627_20170127T231654_015024_0188B3_738D				
S1A_IW_GRDH_1SDV_20170220T231604_20170220T231629_015374_019399_E89C	2017-02-20	IW_GRDH	VV VH	Ascending
S1A_IW_GRDH_1SDV_20170220T231629_20170220T231657_015374_019399_84A0				

S1A_IW_GRDH_1SDV_20170304T231603_20170304T231630_015549_0198E0_2C10	2017-03-04	IW_GRDH	VV VH	Ascending
S1A_IW_GRDH_1SDV_20170304T231629_20170304T231657_015549_0198E0_DBC4				
S1A_IW_GRDH_1SDV_20170316T231604_20170316T231629_015724_019E19_49E2	2017-03-16	IW_GRDH	VV VH	Ascending
S1A_IW_GRDH_1SDV_20170316T231629_20170316T231657_015724_019E19_FF0B				
S1A_IW_GRDH_1SDV_20170328T231605_20170328T231630_015899_01A357_DF8F	2017-03-28	IW_GRDH	VV VH	Ascending
S1A_IW_GRDH_1SDV_20170328T231630_20170328T231657_015899_01A357_0425				
S1A_IW_GRDH_1SDV_20170409T231605_20170409T231630_016074_01A895_B883	2017-04-09	IW_GRDH	VV VH	Ascending
S1A_IW_GRDH_1SDV_20170409T231630_20170409T231658_016074_01A895_752E				
S1A_IW_GRDH_1SDV_20170421T231606_20170421T231631_016249_01ADF0_C782	2017-04-21	IW_GRDH	VV VH	Ascending
S1A_IW_GRDH_1SDV_20170421T231631_20170421T231658_016249_01ADF0_66B4				

Appendix B ROI Summary of Ratio Values

Below are tables of average ROI ratio statistics (mean) for images with potential wet snow in all three years (a) 2014-2015, (b) 2015-2016 and (c) 2016-2017.

(a) Winter 2014-2015

Date	ROI Number	Average HH Ratio [dB]	Average HV Ratio [dB]	Wet or Not
2014.11.22	ROI 1	2.04	0.32	W
	ROI 2	0.38	0.47	W
	ROI 3	-0.75	-0.80	W
	ROI 4	-0.67	1.24	W
	ROI 5	0.32	0.11	
	ROI 6	1.14	0.55	
	ROI 7	1.60	1.70	W
	ROI 8	-1.50	-1.03	W
	ROI 9	-0.11	-3.68	W
	ROI 10	-1.45	0.13	
	ROI 11	-0.29	-0.96	
	ROI 12	-1.90	-1.17	
	ROI 13	-2.05	-2.30	W
	ROI 14	-2.02	-2.05	W
2014.12.16	ROI 1	0.36	2.06	
	ROI 2	0.80	3.23	W
	ROI 3	-1.56	0.62	W
	ROI 4	-0.41	1.12	W
	ROI 5	-1.14	1.72	
	ROI 6	0.25	2.76	W
	ROI 7	-0.41	2.41	
	ROI 8	-0.68	0.88	W
	ROI 9	-1.26	1.54	
	ROI 10	-1.28	-0.29	
	ROI 11	-2.79	0.00	
	ROI 12	-3.09	0.12	
	ROI 13	-4.23	-1.75	
	ROI 14	-2.61	-1.16	W
2014.12.28	ROI 1	1.45	-0.43	
	ROI 2	-0.48	0.36	
	ROI 3	-2.57	-4.99	

	ROI 4	-2.59	-2.44	
	ROI 5	-0.22	0.26	
	ROI 6	-0.12	-1.10	
	ROI 7	-0.57	-3.17	
	ROI 8	-1.14	-0.66	
	ROI 9	0.00	-0.90	W
	ROI 10	-2.32	0.18	W
	ROI 11	-1.25	-2.08	
	ROI 12	-0.81	-1.96	
	ROI 13	-1.39	-2.74	W
	ROI 14	-1.65	-0.85	W

(b) Winter 2016

Date	**ROI Number**	**Average HH Ratio [dB]**	**Average HV Ratio [dB]**	**Wet or Not**
2016.1.25	South ROI 1	-1.05	-2.08	W
	South ROI 2	-1.17	-1.66	
	South ROI 3	-2.51	-2.06	
	South ROI 4	-2.30	-3.06	
	South ROI 5	-1.65	-2.13	
	South ROI 6	-2.46	-3.18	
	Middle ROI 1	-0.56	-2.12	W
	North ROI 1	-1.32	-3.21	
	North ROI 2	-2.29	-2.31	
	North ROI 3	-1.52	-2.10	
	North ROI 4	-1.95	-2.01	
	North ROI 5	-1.08	-0.47	
	North ROI 6	-0.10	-1.00	
	North ROI 7	-5.76	-0.95	
	North ROI 8	-1.08	-1.61	
	North ROI 9	-1.09	-0.77	
	North ROI 10	0.27	-0.84	
2016.3.25	South ROI 1	1.50	0.92	
	South ROI 2	0.24	-0.42	
	South ROI 3	1.63	0.94	
	South ROI 4	-1.02	-0.07	
	South ROI 5	-2.20	-1.20	
	South ROI 6	0.38	-0.24	
	Middle ROI 1	2.34	1.65	
	North ROI 1	0.18	-3.25	

	North ROI 2	1.13	0.46	
	North ROI 3	3.75	3.47	
	North ROI 4	-0.07	-0.65	
	North ROI 5	1.44	-0.73	
	North ROI 6	0.00	-0.82	
	North ROI 7	-2.91	0.55	
	North ROI 8	2.86	3.15	
	North ROI 9	-2.81	-1.05	
	North ROI 10	3.32	2.57	W
2016.4.6	South ROI 1	-0.92	-1.77	W
	South ROI 2	-0.93	-2.01	W
	South ROI 3	-1.77	-1.77	
	South ROI 4	-1.77	-1.72	
	South ROI 5	-2.37	-0.29	
	South ROI 6	0.42	-0.30	
	Middle ROI 1	1.06	-0.26	
	North ROI 1	-3.32	-1.42	
	North ROI 2	0.88	-0.12	
	North ROI 3	0.25	-0.92	
	North ROI 4	-0.40	0.05	
	North ROI 5	0.48	-1.55	
	North ROI 6	-1.19	-1.21	
	North ROI 7	-0.93	-1.68	
	North ROI 8	-0.69	-1.28	
	North ROI 9	0.68	-1.34	
	North ROI 10	0.79	-1.73	

(c) Winter 2016-2017

Date	**ROI Number**	**Average HH Ratio [dB]**	**Average HV Ratio [dB]**	**Wet or Not**
2016.12.22	South ROI 1	-2.41	-2.60	W
	South ROI 2	-2.60	-1.52	W
	South ROI 3	-1.64	-1.46	W
	South ROI 4	-1.28	-0.58	W
	South ROI 5	-3.05	-2.70	W
	South ROI 6	-1.06	-0.65	W
	South ROI 7	-1.70	-4.43	W
	Middle ROI 1	-1.16	-2.28	W
	North ROI 1	-0.59	-0.55	W
	North ROI 2	-3.50	-1.32	W

	North ROI 3	-0.48	-0.72	W
	North ROI 4	-1.88	-3.42	W
	North ROI 5	-1.32	-2.02	W
	North ROI 6	-1.51	-1.05	W
2017.1.3	South ROI 1	1.36	1.97	W
	South ROI 2	0.85	1.83	W
	South ROI 3	1.05	1.76	W
	South ROI 4	0.20	0.26	
	South ROI 5	-2.11	-1.75	W
	South ROI 6	-1.16	-1.38	W
	South ROI 7	-1.22	-1.73	W
	Middle ROI 1	0.62	1.61	W
	North ROI 1	-3.20	-4.77	W
	North ROI 2	-4.02	-4.57	W
	North ROI 3	-0.69	-0.88	W
	North ROI 4	-0.70	-1.94	W
	North ROI 5	-2.71	-4.83	W
	North ROI 6	-1.41	-2.15	W
2017.1.15	South ROI 1	-2.56	-3.34	
	South ROI 2	-2.12	-1.78	
	South ROI 3	-1.92	-1.94	
	South ROI 4	-1.51	-0.97	
	South ROI 5	-2.32	-2.67	
	South ROI 6	-1.48	-2.25	
	South ROI 7	-3.11	-2.22	W
	Middle ROI 1	-2.44	-2.86	
	North ROI 1	-0.99	-2.06	
	North ROI 2	-1.94	-1.72	
	North ROI 3	-0.45	-0.59	W
	North ROI 4	0.03	0.25	
	North ROI 5	-1.02	-1.10	
	North ROI 6	0.84	-0.47	
2017.2.20	South ROI 1	0.73	1.06	
	South ROI 2	0.83	0.51	
	South ROI 3	0.94	0.33	
	South ROI 4	-0.30	-0.31	
	South ROI 5	-0.96	-0.38	
	South ROI 6	-0.37	0.15	W
	South ROI 7	-3.57	-3.95	W
	Middle ROI 1	-0.37	-0.93	

	North ROI 1	-2.01	-1.88	W
	North ROI 2	-4.13	-2.72	W
	North ROI 3	-0.66	-0.49	W
	North ROI 4	-1.58	-2.75	W
	North ROI 5	-2.60	-3.96	W
	North ROI 6	-1.57	-1.30	W
2017.4.9	South ROI 1	-0.33	-0.07	
	South ROI 2	-1.18	-0.82	
	South ROI 3	1.37	0.86	
	South ROI 4	0.73	0.59	
	South ROI 5	-0.42	-0.47	
	South ROI 6	1.37	1.40	
	South ROI 7	-1.86	-1.48	
	Middle ROI 1	-0.06	-1.18	
	North ROI 1	0.51	0.10	
	North ROI 2	-1.69	0.85	
	North ROI 3	0.80	0.61	W
	North ROI 4	-0.63	-2.06	W
	North ROI 5	-0.06	0.50	W
	North ROI 6	1.50	1.35	W

Appendix C Confusion Matrix for Thresholds

(a) -2.5 dB Threshold

1) 2014-2015 HH Images

Ratio / Ground Reference	Ratio<-2.5 dB	Ratio>-2.5dB	Total
Wet	1	18	19
Not Wet	4	19	23

2) 2014-2015 HV Images

Ratio / Ground Reference	Ratio<-2.5 dB	Ratio>-2.5dB	Total
Wet	2	17	19
Not Wet	2	21	23

3) 2015-2016 HH Images

Ratio / Ground Reference	Ratio<-2.5 dB	Ratio>-2.5dB	Total
Wet	0	5	5
Not Wet	6	40	46

4) 2015-2016 HV Images

Ratio / Ground Reference	Ratio<-2.5 dB	Ratio>-2.5dB	Total
Wet	1	4	5
Not Wet	1	43	46

5) 2016-2017 VV Images

Ratio / Ground Reference	Ratio<-2.5 dB	Ratio>-2.5dB	Total
Wet	8	32	40
Not Wet	1	29	30

6) 2016-2017 VH Images

Ratio / Ground Reference	Ratio<-2.5 dB	Ratio>-2.5dB	Total
Wet	11	29	40
Not Wet	2	28	30

(b) -2 dB Threshold

1) 2014-2015 HH Images

Ratio / Ground Reference	Ratio<-2 dB	Ratio>-2dB	Total
Wet	6	13	19
Not Wet	4	19	23

2) 2014-2015 HV Images

Ratio / Ground Reference	Ratio<-2 dB	Ratio>-2 dB	Total
Wet	3	16	19
Not Wet	3	20	23

3) 2015-2016 HH Images

Ratio / Ground Reference	Ratio<-2 dB	Ratio>-2 dB	Total
Wet	0	5	5
Not Wet	9	37	46

4) 2015-2016 HV Images

Ratio / Ground Reference	Ratio<-2 dB	Ratio>-2 dB	Total
Wet	3	2	5
Not Wet	4	42	46

5) 2016-2017 VV Images

Ratio / Ground Reference	Ratio<-2 dB	Ratio>-2 dB	Total
Wet	12	28	40
Not Wet	4	26	30

6) 2016-2017 VH Images

Ratio / Ground Reference	Ratio<-2 dB	Ratio>-2 dB	Total
Wet	16	24	40
Not Wet	4	26	30

(c) -1.5 dB Threshold

1) 2014-2015 HH Images

Ratio / Ground Reference	Ratio<-1.5 dB	Ratio>-1.5dB	Total
Wet	8	11	19
Not Wet	6	17	23

2) 2014-2015 HV Images

Ratio / Ground Reference	Ratio<-1.5 dB	Ratio>-1.5dB	Total
Wet	3	16	19
Not Wet	3	20	23

3) 2015-2016 HH Images

Ratio / Ground Reference	Ratio<-1.5 dB	Ratio>-1.5dB	Total
Wet	0	5	5
Not Wet	13	33	46

4) 2015-2016 HV Images

Ratio / Ground Reference	Ratio<-1.5 dB	Ratio>-1.5dB	Total
Wet	4	1	5
Not Wet	14	32	46

5) 2016-2017 VV Images

Ratio / Ground Reference	Ratio<-1.5 dB	Ratio>-1.5dB	Total
Wet	18	22	40
Not Wet	9	21	30

6) 2016-2017 VH Images

Ratio / Ground Reference	Ratio<-1.5 dB	Ratio>-1.5dB	Total
Wet	21	19	40
Not Wet	7	23	30

(d) -1 dB Threshold

1) 2014-2015 HH Images

Ratio / Ground Reference	Ratio<-1 dB	Ratio>-1dB	Total
Wet	9	10	19
Not Wet	12	11	23

2) 2014-2015 HV Images

Ratio / Ground Reference	Ratio<-1 dB	Ratio>-1dB	Total
Wet	6	13	19
Not Wet	8	15	23

3) 2015-2016 HH Images

Ratio / Ground Reference	Ratio<-1 dB	Ratio>-1dB	Total
Wet	1	4	5
Not Wet	22	24	46

4) 2015-2016 HV Images

Ratio / Ground Reference	Ratio<-1 dB	Ratio>-1dB	Total
Wet	4	1	5
Not Wet	23	23	46

5) 2016-2017 VV Images

Ratio / Ground Reference	Ratio<-1 dB	Ratio>-1dB	Total
Wet	26	14	40
Not Wet	12	18	30

6) 2016-2017 VH Images

Ratio / Ground Reference	Ratio<-1 dB	Ratio>-1dB	Total
Wet	26	14	40
Not Wet	11	19	30

(e) -0.5 dB Threshold

1) 2014-2015 HH Images

Ratio / Ground Reference	Ratio<-0.5 dB	Ratio>-0.5 dB	Total
Wet	9	10	19
Not Wet	12	11	23

2) 2014-2015 HV Images

Ratio / Ground Reference	Ratio<-0.5 dB	Ratio>-0.5 dB	Total
Wet	6	13	19
Not Wet	8	15	23

3) 2015-2016 HH Images

Ratio / Ground Reference	Ratio<-0.5 dB	Ratio>-0.5 dB	Total
Wet	4	1	5
Not Wet	20	26	46

4) 2015-2016 HV Images

Ratio / Ground Reference	Ratio<-0.5 dB	Ratio>-0.5 dB	Total
Wet	4	1	5
Not Wet	30	36	46

5) 2016-2017 VV Images

Ratio / Ground Reference	Ratio<-0.5 dB	Ratio>-0.5 dB	Total
Wet	29	11	40
Not Wet	15	14	30

6) 2016-2017 VH Images

Ratio / Ground Reference	Ratio<-0.5 dB	Ratio>-0.5 dB	Total
Wet	31	9	40
Not Wet	15	15	30